Designing High-Fidelity Zeno Gates for Dissipative Cat Qubits

Ronan Gautier, Mazyar Mirrahimi, Alain Sarlette

Designing High-Fidelity Zeno Gates for Dissipative Cat Qubits

Ronan Gautier,[1,*] Mazyar Mirrahimi,[1] and Alain Sarlette[1,2]

[1] *Laboratoire de Physique de l'École Normale Supérieure, Inria, ENS, Mines ParisTech, Université Paris Sciences et Lettres (PSL), Sorbonne Université, Paris France*

[2] *Department of Electronics and Information Systems, Ghent University, 9052 Ghent, Belgium*

(Received 27 March 2023; revised 21 July 2023; accepted 20 September 2023; published 25 October 2023)

Bosonic cat qubits stabilized with a driven two-photon dissipation are systems with exponentially biased noise, opening the door to low-overhead, fault-tolerant, and universal quantum computing. However, current gate proposals for such qubits induce substantial noise of the unprotected type, the poor scaling of which with the relevant experimental parameters limits their practical use. In this work, we provide a new perspective on dissipative cat qubits by reconsidering the reservoir mode used to engineer the tailored two-photon dissipation and showing how it can be leveraged to mitigate gate-induced errors. Doing so, we introduce four new designs of high-fidelity and bias-preserving cat-qubit gates and compare them to the prevalent gate methods. These four designs should give a broad overview of gate engineering for dissipative systems with different and complementary ideas. In particular, we propose both already achievable low-error gate designs and longer-term implementations.

DOI: 10.1103/PRXQuantum.4.040316

I. INTRODUCTION

The promise of quantum computing relies on the unpleasant predicament that a quantum system should be freely controllable but also very long lived, two often conflicting requirements. To overcome this issue, a promising path toward fault-tolerance is quantum error correction [1–5] with discrete-variable qubits. By redundantly encoding information, the eventual computational errors induced by environment noise can be resolved and corrected [6–10]. While the control of most discrete-variable qubits is now well established [11–16], they are often error prone by construction. For this reason, continuous-variable codes [17–23] are attracting increasing interest due to their inherent robustness to errors and promise of low-overhead experimental setups [24–28].

In particular, bosonic cat qubits are encoded in opposite-phase coherent states of a quantum harmonic oscillator [29–34]. When stabilized with a driven two-photon dissipation, the so-called *bit-flip* error, consisting of flipping one computational state to the other, is exponentially suppressed with the mean number of photons in each coherent state. This can be viewed as a form of autonomous error correction, in which detection and correction of bit-flip errors is performed by a tailored interaction with the environment [35–41]. Exponentially large coherent-state lifetimes have thus been demonstrated for dissipative cat qubits [42,43].

The next key ingredient toward a hardware-efficient and fault-tolerant quantum processor based on cat qubits is to demonstrate single- and two-qubit physical gates that preserve the exponential protection against bit flips [44–48]. Besides this bit-flip suppression, these gates should admit *phase-flip* errors well below the threshold of a discrete-variable error-correcting code used for phase-flip correction, such as the repetition code. To this aim, several proposals have been put forward recently to improve the fidelity of cat-qubit gates [49–51], with the respective benefits and feasibility strongly depending on the particular experimental setup envisioned.

The present work follows the lines of these research efforts, proposing alternatives the performance of which is competitive in at least some contexts and that may sometimes be naturally combined with these other strategies. We thus introduce four new designs for $Z(\theta)$, controlled-NOT (CNOT), and Toffoli gates on dissipatively stabilized cat qubits to help mitigate the incoherent phase errors induced by those gates. Indeed, while the prevalent method of gate engineering based on the Zeno effect [30,36] has the great benefit of simplicity, it also features relatively large gate errors and a poor scaling with the relevant experimental parameters that may limit its practical use [37].

*Corresponding author. ronan.gautier@inria.fr

To answer this limitation, our main approach is to reduce the logical information that the two-photon dissipation carries away to the environment under Zeno driving and that induces phase-flip back action. Our first two designs maintain the same Zeno drives and interaction with the buffer mode mediating two-photon dissipation but they feed information back from the buffer state to the cat-qubit system before it can leak out to the environment. With this principle, we have been able to improve gate fidelities by up to 2 orders of magnitude with realistic experimental parameters. Our other two designs instead modify the Zeno-gate drive, to avoid pushing any information from the cat qubit to the dissipative buffer in the first place. One solution, based on locally flat Hamiltonians, promises a polynomial improvement in the scaling of gate errors with the cat size. Our final design demonstrates exponentially small $Z(\theta)$ gate errors with a tailored dissipation to an ancillary qubit. While its generalization to CNOT gates is beyond the current state of the art, it provides a new way to leverage dissipation for gate engineering.

The paper is organized as follows. We begin in Sec. II by reviewing dissipative cat qubits and the implementation of their standard gates. In Sec. III, we provide a new perspective on the origin of gate errors using the buffer mode. Section IV gives a short summary of the different gate-error-mitigation designs introduced in this paper. And, finally, each design is detailed separately in Secs. V–VIII. We conclude in Sec. IX.

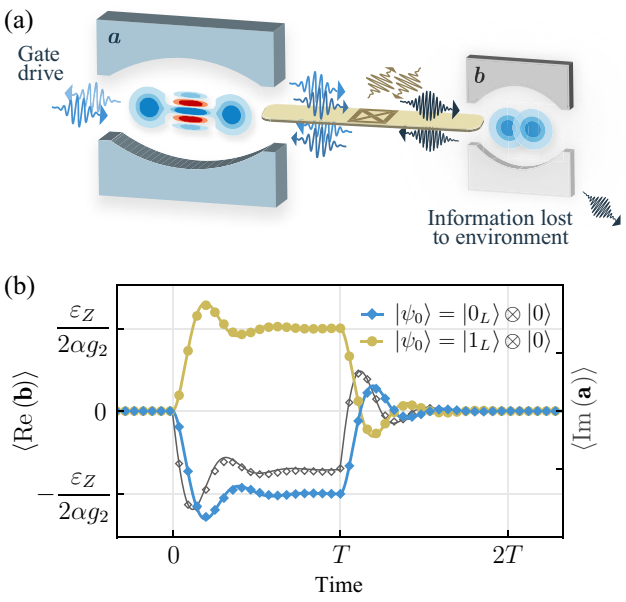

FIG. 1. (a) Cat-qubit mode a stabilized by a two-to-one photon exchange with buffer mode b, mediated by a nonlinear circuit element (middle). The gate drive, by displacing the cat mode, induces a small splitting of the buffer mode conditioned on the cat state. Information is then lost to the environment through the high damping rate of the buffer, hence inducing incoherent gate errors. (b) The average displacement of the buffer (color, left scale) and cat mode (black, right scale) before, during, and after a Zeno $Z(\pi)$ gate of duration T, with a cat mode initialized in $|0_L/1_L\rangle \approx |\pm\alpha\rangle$ and the buffer initialized in vacuum. The markers show numerical data obtained from integration of the full master equation. The lines show Eq. (16).

II. REVIEW OF CAT-QUBIT GATES

A. Stabilization and encoding

In the dissipative stabilization of cat qubits, a harmonic oscillator exchanges pairs of photons with its environment both through a driven dissipation process and a two-photon pump. The Lindblad master equation that governs this oscillator is

$$\frac{d\boldsymbol{\rho}}{dt} = \kappa_2 \mathcal{D}[\mathbf{a}^2 - \alpha^2]\boldsymbol{\rho}, \tag{1}$$

where $\mathcal{D}[\mathbf{L}]\boldsymbol{\rho} = \mathbf{L}\boldsymbol{\rho}\mathbf{L}^\dagger - \{\mathbf{L}^\dagger\mathbf{L}, \boldsymbol{\rho}\}/2$ is the dissipation superoperator, $\mathbf{a}$ denotes the annihilation operator of the cat-qubit mode, κ_2 is the rate of two-photon dissipation, and α is the cat-qubit amplitude. Throughout this paper, we assume $\alpha \in \mathbb{R}$ unless specified otherwise. To engineer this unusual dissipation, an ancillary buffer mode—not necessarily harmonic—is often introduced to mediate the exchange of photon pairs between the oscillator and its environment, as depicted in Fig. 1(a). This results in a two-mode Lindblad master equation,

$$\frac{d\boldsymbol{\rho}}{dt} = -i\,[\mathbf{H}_{AB}, \boldsymbol{\rho}] + \kappa_b \mathcal{D}[\mathbf{b}]\boldsymbol{\rho}, \tag{2}$$

where $\mathbf{H}_{AB} = g_2(\mathbf{a}^2 - \alpha^2)\mathbf{b}^\dagger + \text{h.c.}$ is a driven two-to-one photon exchange Hamiltonian, in which $\mathbf{b}$ is the annihilation operator of the ancillary buffer mode. In the limit of $\kappa_b \gg g_2$, this additional mode can be adiabatically eliminated [52,53] to retrieve the single-mode model of Eq. (1) with a typical two-photon loss rate $\kappa_2 \equiv 4g_2^2/\kappa_b$. Both systems feature a degenerate subspace of steady states of dimension 2, in which the cat qubit is encoded. In the single-mode system, the associated code words of this qubit are defined as

$$\begin{aligned} |0_L\rangle &\equiv \frac{1}{\sqrt{2}}\left(|\mathcal{C}_\alpha^+\rangle + |\mathcal{C}_\alpha^-\rangle\right) = |\alpha\rangle + \mathcal{O}(e^{-2|\alpha|^2}), \\ |1_L\rangle &\equiv \frac{1}{\sqrt{2}}\left(|\mathcal{C}_\alpha^+\rangle - |\mathcal{C}_\alpha^-\rangle\right) = |-\alpha\rangle + \mathcal{O}(e^{-2|\alpha|^2}), \end{aligned} \tag{3}$$

where $|\pm\alpha\rangle$ are opposite-phase coherent states and $|\mathcal{C}_\alpha^\pm\rangle \equiv \mathcal{N}_\pm(|\alpha\rangle \pm |-\alpha\rangle)$ are Schrödinger-cat states of even and odd photon-number parity.

This dissipative stabilization of cat qubits is quite remarkable for its biased robustness to errors that are local in phase space, whether they may come from

spurious Hamiltonians—e.g., neglected in some underlying rotating-wave approximation—or undesired couplings of the oscillator to its environment. Indeed, due to the coherent states being localized on opposite sides of phase space, it is expected that the bit-flip error rate Γ_X of a dissipative cat qubit is suppressed exponentially in the cat mean number of photons $|\alpha|^2$, according to $\Gamma_X = \Gamma_{X,0}\exp\left(-2|\alpha|^2\right)$ [30,42]. Although difficult to compute, the prefactor $\Gamma_{X,0}$ typically depends on terms that cause leakage out of the qubit code space and may vary during the operation of the device. On the contrary, the qubit phase information is encoded in the photon-number parity. This degree of freedom is not protected by the stabilization mechanism and it typically becomes linearly more fragile as the cat mean number of photons $|\alpha|^2$ increases. Hence, the idea behind cat qubits is to benefit from the exponential hardware protection against bit flips and to concentrate error-correction efforts on phase flips with hopefully low enough error rates.

B. Bias-preserving gates

For this paradigm to work, the noise bias must be preserved when operating gates on the physical qubits, meaning that we should never convert phase errors into bit errors (or introduce significant bit errors in any other ways). In Ref. [36], a set of bias-preserving physical operations is proposed for universal quantum computation with cat qubits. This set comprises Pauli-X, $Z(\theta)$ rotations, CNOT, and Toffoli gates, in addition to the preparation and measurement of cat states in the orthonormal basis $|\pm_L\rangle = \left|\mathcal{C}_\alpha^{\pm}\right\rangle$. Such a gate set allows for forward concatenation with various logical error-correcting codes such as the repetition code [36], the $XZZX$ code [9], or a rectangular surface code [37]. In the remainder of this section, we highlight some physical gate-design elements that will be useful for this paper; a more complete review can be found in Ref. [36].

1. Pauli-X

The Pauli-X gate corresponds to a π phase delay on the oscillator or, equivalently, to a cat-qubit code-space rotation in phase space for some time $T = \pi/\Delta$, where 2Δ is the buffer frequency detuning with respect to the cat-qubit frame. This exchanges the two computational basis states. From a complementary viewpoint, the engineered dynamics should stabilize the cat-qubit code space with Eq. (1) but in a frame that rotates at the detuned frequency. Working this back to the cat-qubit frame, we see that we must engineer the dynamics of

$$\frac{d\boldsymbol{\rho}}{dt} = -i[\Delta\mathbf{a}^\dagger\mathbf{a}, \boldsymbol{\rho}] + \kappa_2\mathcal{D}[\mathbf{a}^2 - \alpha^2 e^{-2i\Delta t}]\boldsymbol{\rho}. \tag{4}$$

Since this master equation preserves photon parity, no phase errors are induced by this gate design.

While the implementation of both terms of Eq. (4) is well established, one can in principle choose to engineer only one of the two terms. If only the second term of Eq. (4) is kept, the cat state is pulled by the time-varying set point of the dissipation, incurring negligible leakage and bit flips for a sufficiently slow code-space rotation. With the Hamiltonian alone, the rotation is performed exactly but the stabilizing effect of two-photon dissipation is turned off during the gate. For fast-enough gates, however, the design is still bias preserving under local errors and code-space leakage can be suppressed after the gate, once stabilization is turned back on.

2. Z(θ) rotations

Cat-qubit $Z(\theta)$ rotations require the accumulation of a different phase on the $|\alpha\rangle$ and $|-\alpha\rangle$ components of the code space. Since this exact evolution is not directly accessible by simple experimental means, the standard proposal is an approximate one based on the Zeno effect. The combination of a small drive displacing the state in phase space and of the dominant dissipation of Eq. (1) pulling the state back to the code space induces to first order an effective phase shift inside a slightly deformed code space, and hence the desired gate [30]. The master equation to be engineered takes the standard form,

$$\frac{d\boldsymbol{\rho}}{dt} = -i[\mathbf{H}_Z, \boldsymbol{\rho}] + \kappa_2\mathcal{D}[\mathbf{a}^2 - \alpha^2]\boldsymbol{\rho}, \tag{5}$$

with, for real-valued α, a drive Hamiltonian

$$\mathbf{H}_Z \equiv \varepsilon_Z(\mathbf{a}^\dagger + \mathbf{a}), \tag{6}$$

for which the gate angle reads $\theta = 4\alpha\int\varepsilon_Z dt$. To second order, the Zeno effect involves phase decoherence that scales as $(\varepsilon_Z/\kappa_2)^2$, as discussed more extensively in Sec. III.

3. CNOT and Toffoli

By definition, a CNOT gate is a Pauli-X gate on a target qubit conditioned on the state of a control qubit along its Z axis or, equivalently, a Pauli-Z gate on a control qubit conditioned on the state of a target qubit along its X axis. Therefore, the standard design of CNOT or Toffoli gates for cat qubits involves a combination of the X- and Z-gate implementations and of their respective issues. From the viewpoint of the X gate, the dynamics of Eq. (4) should be applied conditionally on the computational state of a control qubit. As introduced in Ref. [36], this can be done with the two-mode master equation

$$\frac{d\boldsymbol{\rho}}{dt} = -i[\mathbf{H}_{\mathrm{CX}}, \boldsymbol{\rho}] + \kappa_2\mathcal{D}[\mathbf{L}_C]\boldsymbol{\rho} + \kappa_2\mathcal{D}[\mathbf{L}_T(t)]\boldsymbol{\rho}, \tag{7}$$

where $\mathbf{L}_C \equiv \mathbf{a}_C^2 - \alpha^2$ is the standard two-photon dissipation of Eq. (1) on the control qubit, $\mathbf{L}_T(t)$ is a time-dependent dissipation on the target qubit,

$$\mathbf{L}_T(t) \equiv \mathbf{a}_T^2 - \frac{\alpha}{2}(\mathbf{a}_C + \alpha) + \frac{\alpha}{2}(\mathbf{a}_C - \alpha)e^{-2i\Delta t}, \quad (8)$$

and the coupling Hamiltonian reads

$$\mathbf{H}_{CX} \equiv \varepsilon_{CX}(\mathbf{a}_C^\dagger + \mathbf{a}_C - 2\alpha)(\mathbf{a}_T^\dagger \mathbf{a}_T - n_p). \quad (9)$$

Here, $\mathbf{a}_{C/T}$ denote the control- and target-qubit modes, respectively, n_p is any even integer close to $|\alpha|^2$, and $\varepsilon_{CX}(t) = \Delta(t)/4\alpha$. Adding a second control mode in Eqs. (8) and (9) yields the Toffoli-gate operators. Similarly to the X gate, the Hamiltonian of Eq. (9) may be dropped to ease the experimental requirements as long as the set point of the dissipation in Eq. (8) rotates slowly enough to adiabatically pull the state. Alternatively, the dissipation of Eq. (8) can also be dropped, in which case the Hamiltonian of Eq. (9) alone induces the intended target-qubit rotation but at the cost of turning off target-qubit stabilization temporarily during the gate.

The viewpoint of the Z gate clarifies the impact of conditioning on the control qubit. The link is most direct when the dissipator of Eq. (8) is dropped, as proposed in Ref. [50]. Indeed, the Hamiltonian of Eq. (9), together with the two-photon dissipation in Eq. (1) on the control qubit, amounts to the same Zeno dynamics as for the $Z(\theta)$ rotation, the only difference being that the drive amplitude ε_Z in Eq. (6) is now conditioned on the photon number in the target-qubit state. This achieves the required gate since, at first order, the control qubit undergoes an even number of $Z(\pi)$ gates for all even Fock states of the target qubit and, respectively, an odd number of $Z(\pi)$ gates for all odd Fock states, hence refocusing on the even and odd cat code spaces at the end of the CNOT gate. At second order though, we see that as for the Z gate, the process induces phase decoherence on the control cat qubit.

4. Gate errors

During each of these gates, there are two main effects that induce phase errors. The first is spontaneous emission of photons from the oscillator, with dissipation operator $\mathcal{D}[\mathbf{a}]$. This causes phase errors linearly in time and in $|\alpha|^2$ independently of the ongoing gate and also results in correlated errors for multiqubit gates [37]. Since this source of decoherence can only be mitigated by increasing the oscillator lifetime or by changing the overall qubit encoding, it will not be considered any further in this paper. However, it could in principle feature nontrivial dynamics once combined with gate proposals, so a complete model of errors is studied in Appendix B. In addition, single-photon losses motivate the need for faster gate operations (thus increasing the overall fidelities) and limits the benefits granted by increasing $|\alpha|^2$.

Phase errors are also induced directly by gate processes but only on modes for which parity-switching dynamics are engineered. In particular, target qubits of multiqubit gates do not suffer from such errors and hence most of the dynamics of interest occur on control qubits. Consequently, $Z(\theta)$-rotation gates provide much of the important physics and strategies to mitigate cat-qubit gate errors can all be understood within the scope of this single-qubit gate. This paper is therefore devoted to the mitigation of gate-induced errors and always begins with the design of $Z(\theta)$ gates before generalizing.

III. ZENO-GATE ERRORS

To illustrate the origin of gate-induced errors and how they can be mitigated by tampering with the ancillary buffer mode, let us consider the full Hamiltonian engineered for $Z(\theta)$ gates in the presence of the buffer mode,

$$\mathbf{H} = \mathbf{H}_{AB} + \mathbf{H}_Z. \quad (10)$$

Together with the high damping rate of the buffer, the first term mediates the two-photon dissipation while the second term drives the required gate. Let us move into the shifted Fock basis as introduced in Ref. [37] (see also Appendix A for a short review). This change of basis reads

$$\mathbf{a} \to \boldsymbol{\sigma}_z \otimes (\tilde{\mathbf{a}} + \alpha) \quad (11)$$

and effectively represents a displaced oscillator, where the displacement is conditional on $\boldsymbol{\sigma}_z$, the Pauli operator corresponding to the cat-qubit logical state. This change of basis is nonorthonormal and approaches degeneracy at high Fock states but it is sufficiently close to a regular change of coordinates for states close to $|\pm\alpha\rangle$ and thus adequate for our investigation of local errors in the short time limit. Then, $\tilde{\mathbf{a}}$ is a gauge mode that models a local oscillator around the $|\pm\alpha\rangle$ coherent states; in particular, $\tilde{\mathbf{a}}$ in vacuum is equivalent to being perfectly inside the cat-qubit encoding space. With this definition, the Hamiltonian of Eq. (10) reads ($\alpha \in \mathbb{R}$)

$$\tilde{\mathbf{H}} = g_2(\tilde{\mathbf{a}}^2 + 2\alpha\tilde{\mathbf{a}})\mathbf{b}^\dagger + \varepsilon_Z \boldsymbol{\sigma}_z(\tilde{\mathbf{a}}^\dagger + \alpha) + \text{h.c.}. \quad (12)$$

The ideal Hamiltonian that implements the $Z(\theta)$ rotation of the qubit (and nothing else) now appears as the term $(\alpha\varepsilon_Z\boldsymbol{\sigma}_z + \text{h.c.})$. In the following, we move into the rotating frame of this Pauli Hamiltonian to simplify the analysis. In addition, in the limit of a small Zeno drive, the effective displacements on the gauge mode $\tilde{\mathbf{a}}$ and on the buffer mode $\mathbf{b}$ are small, such that we can neglect the second-order term $\tilde{\mathbf{a}}^2\mathbf{b}^\dagger + \text{h.c.}$. The corresponding Hamiltonian thus reads

$$\tilde{\mathbf{H}}' \approx 2\alpha g_2 \tilde{\mathbf{a}}\mathbf{b}^\dagger + \varepsilon_Z \boldsymbol{\sigma}_z \tilde{\mathbf{a}}^\dagger + \text{h.c.}. \quad (13)$$

Writing the master equation with the Hamiltonian of Eq. (13) and in the Heisenberg picture [54] for both $\tilde{\mathbf{a}}$ and

b yields a set of coupled equations,

$$\dot{\tilde{\mathbf{a}}} = -2i\alpha g_2 \mathbf{b} - i\varepsilon_Z \boldsymbol{\sigma}_z, \tag{14a}$$

$$\dot{\mathbf{b}} = -2i\alpha g_2 \tilde{\mathbf{a}} - \kappa_b \mathbf{b}/2. \tag{14b}$$

Decoupling these equations gives the second-order differential equations

$$\ddot{\tilde{\mathbf{a}}} + \tfrac{1}{2}\kappa_b \dot{\tilde{\mathbf{a}}} + \nu^2 \tilde{\mathbf{a}} = -\tfrac{i}{2}\kappa_b \varepsilon_Z \boldsymbol{\sigma}_z - i\dot{\varepsilon}_Z \boldsymbol{\sigma}_z, \tag{15a}$$

$$\ddot{\mathbf{b}} + \tfrac{1}{2}\kappa_b \dot{\mathbf{b}} + \nu^2 \mathbf{b} = -\nu \varepsilon_Z \boldsymbol{\sigma}_z, \tag{15b}$$

where $\nu \equiv 2\alpha g_2$ and we have used that $d\boldsymbol{\sigma}_z/dt = 0$ since $\boldsymbol{\sigma}_z$ commutes with Eq. (13). Finally, making the inverse change of basis on the cat-qubit mode, i.e., $\boldsymbol{\sigma}_z \otimes (\tilde{\mathbf{a}} + \alpha) \to \mathbf{a}$ yields

$$\ddot{\mathbf{a}} + \tfrac{1}{2}\kappa_b \dot{\mathbf{a}} + \nu^2 \mathbf{a} = \nu^2 \alpha \boldsymbol{\sigma}_z - \tfrac{i}{2}\kappa_b \varepsilon_Z - i\dot{\varepsilon}_Z, \tag{16a}$$

$$\ddot{\mathbf{b}} + \tfrac{1}{2}\kappa_b \dot{\mathbf{b}} + \nu^2 \mathbf{b} = -\nu \varepsilon_Z \boldsymbol{\sigma}_z. \tag{16b}$$

Both the cat-qubit and buffer mode are thus described by a damped harmonic oscillator equation with natural frequency ν and damping rate $\kappa_b/2$. These oscillators are further driven out of equilibrium by the ε_Z drive.

On the cat-qubit mode, we naturally find that equilibrium is given by $\mathbf{a}_{\text{eq}} = \alpha \boldsymbol{\sigma}_z$ when $\varepsilon_Z = 0$, which corresponds to the computational states of cat qubits up to exponentially small corrections that have been neglected by introducing the shifted Fock basis. We also find that, for $\varepsilon_Z > 0$, the mode is displaced along the $\langle \text{Im}(\mathbf{a}) \rangle$ quadrature independently of $\boldsymbol{\sigma}_z$, as expected.

On the buffer mode, it is quite interesting to note that the right-hand-side term is proportional to $\boldsymbol{\sigma}_z$, such that the buffer mode is displaced in opposite directions depending on the computational state of the cat-qubit mode. In other words, the equilibrium position for the buffer mode is $\mathbf{b}_{\text{eq}} = -\varepsilon_Z/\nu \boldsymbol{\sigma}_z$ and, more importantly, $\mathbf{b} \propto \boldsymbol{\sigma}_z$ at all times. Because the buffer mode is largely damped, the environment obtains information about the state of the cat-qubit mode through this effect. As a consequence, measurement of the bit value by the environment dissolves the information contained in the superposition of these bit states and thus induces phase errors. In fact, it is simple to rederive the well-known result of the $Z(\theta)$ gate nonadiabatic error rate by replacing $\mathbf{b}$ with $\mathbf{b}_{\text{eq}}$ in the dissipator of Eq. (2) and integrating over the gate duration. This yields

$$p_Z = p_Z^{(0)} \equiv \frac{\theta^2}{16|\alpha|^4 T} \frac{\kappa_b}{4g_2^2}, \tag{17}$$

which is the same result as in Ref. [37], with $\kappa_2 \equiv 4g_2^2/\kappa_b$.

In Fig. 1(b), we show the average displacement of the buffer mode along the $\langle \text{Re}(\mathbf{b}) \rangle$ quadrature before, during, and after a $Z(\pi)$ gate of duration T. Depending on the initial state of the cat-qubit mode, either $|0_L\rangle$ (blue) or $|1_L\rangle$ (yellow), the buffer mode is displaced in one direction or the other. In fact, we observe the dynamics of a damped oscillator with equilibrium position $\mathbf{b}_{\text{eq}} = \pm\varepsilon_Z/\nu$ for $0 < t < T$ and $\mathbf{b}_{\text{eq}} = 0$ for $t > T$, in excellent agreement with our analysis based on the approximate model of Eq. (16). The displacement of the cat-qubit mode is also shown in black and is independent of the initial state, as expected.

This derivation is meant to provide intuition to the reader about the origin of gate errors. With this intuition in mind, the following sections will introduce multiple gate designs to reduce the errors induced by cat-qubit Zeno dynamics, beginning with a summary.

IV. SUMMARY OF GATE DESIGNS

With the analysis of the previous section in mind, we understand that the loss of phase information during gates is due to the conditional displacement of the buffer mode, which is then measured by the environment. This is indeed the only nonunitary channel and hence it is how quantum information can be lost. Compared to a system with no ancillary buffer in which the information would be directly lost to the environment, the delay provided by the buffer mode can be exploited to reduce gate-induced phase errors without tampering with the ongoing gate.

In this paper, we introduce two methods that rely on kicking back qubit information that has been transferred into the buffer mode and two methods that rely on the reduction of information transfer to the buffer mode in the first place. They are all summarized in Table I, along with the regular Zeno-based gate of Ref. [30] and the combined confinement method that we have recently proposed in Ref. [50]. Although the table only tackles these methods within the scope of the $Z(\theta)$ gate, they can all be generalized to multiqubit gates and the aim is to represent a wide range of ideas for the mitigation of dissipative cat-qubit gate errors. Furthermore, some of these ideas can, in principle, be combined to attain even higher fidelities.

A. Buffer photodetection with classical feedback

In the first method, detailed in Sec. V, the principle is to retrieve the information leaking out by directly measuring the field coming out of the buffer mode, instead of letting it get lost to the environment. An appropriate feedback action can then restore this information back into the cat-qubit system. The measurement is a photon counter. The feedback action corresponds to additional Pauli-Z gates performed either in software or through a modification of the gate drive amplitude and/or duration. Alternatively, one can pursue a heralded gate. An immediate limitation of this technique is the detector efficiency, which will

TABLE I. A comparison of the different designs of $Z(\theta)$ gates for dissipative cat qubits. All designs but the last one can be generalized to two- and three-qubit CNOT and Toffoli gates. For the second and last designs, $\boldsymbol{\sigma}_+$ denotes a Pauli creation operator on some ancillary qubit. $\mathbf{H}_{AB}$ and $\mathbf{H}_Z$ are defined in Eqs. (2) and (6), respectively, and $\mathbf{a}_\theta = \sin(\theta/2)\mathbf{a} + i\cos(\theta/2)\alpha$. In the last column, p_Z denotes the probability of gate errors over a single $Z(\pi)$ gate of duration T.

		Hamiltonian $\mathbf{H}$	Dissipator $\mathcal{D}$	Gate errors
Refs. [30,37]	Standard Zeno	$\mathbf{H}_{AB} + \mathbf{H}_Z$	$\kappa_b\mathcal{D}[\mathbf{b}]$	$p_Z^{(0)} \equiv \frac{\pi^2}{16\lvert\alpha\rvert^4 T}\frac{\kappa_b}{4g_2^2}$
Ref. [50]	Combined dissipation and TPE Hamiltonian	$\mathbf{H}_{AB} + \mathbf{H}_Z + \mathbf{H}_{TPE}$ with $\mathbf{H}_{TPE} \equiv g_2'(\mathbf{a}^2 - \alpha^2)\boldsymbol{\sigma}_+ + \text{h.c.}$	$\kappa_b\mathcal{D}[\mathbf{b}]$	$p_Z = \frac{1}{1+(2g_2'/\kappa_2)^2}p_Z^{(0)}$
Sec. V	Buffer photodetection with classical feedback	$\mathbf{H}_{AB} + \mathbf{H}_Z$	$\kappa_b\mathcal{D}[\mathbf{b}]$ (photodetected)	$p_Z \gtrsim (1-\eta)p_Z^{(0)}$ (detection efficiency η)
Sec. VI	Cat-buffer autonomous feedback	$\mathbf{H}_{AB} + \mathbf{H}_Z$	$\kappa_{ab}\mathcal{D}[\mathbf{ab}]$	$p_Z = \mu\, p_Z^{(0)}$ with $\mu \gtrsim 0.02$
Sec. VII	Locally flat Hamiltonian	$\mathbf{H}_{AB} + \mathbf{H}_{Z,N}$ with $\mathbf{H}_{Z,N} = \varepsilon_Z \sum_{n=0}^{N} c_n(\mathbf{a}+\mathbf{a}^\dagger)^{2n+1}$	$\kappa_b\mathcal{D}[\mathbf{b}]$	$p_Z = \nu\lvert\alpha\rvert^{-2N}p_Z^{(0)}$ with $\nu \sim 1$
Sec. VIII	Discrete jump	$\mathbf{H}_{AB}$	$\kappa_b\mathcal{D}[\mathbf{b}] + \kappa_Z\mathcal{D}[\mathbf{a}_\theta\boldsymbol{\sigma}_+]$	$p_Z = \exp\left(-\kappa_Z\lvert\alpha\rvert^2 T\right)$

directly limit the proportion of information loss that we can counter with respect to Eq. (17). Despite this limitation, this method could become viable with the rapid improvement in circuit-integrated photodetectors and is in any case instructive for the following design.

B. Cat-buffer autonomous feedback

A second method based on the buffer information is presented in Sec. VI. The idea is again that feedback on the cat-qubit photon-number parity is applied after detection of a buffer-mode photon. However, instead of actually applying a measurement and action, this loop is now applied autonomously due to a tailored-dissipation operator. This tailored dissipation takes the form $\mathcal{D}[\mathbf{ab}]$, such that any time, the buffer can lose a photon to the environment—and by doing so can swap the cat-qubit parity, as we have shown in Sec. III: a second parity switch is applied on the cat qubit through the loss of a single cavity photon. With this autonomous feedback, the "detection efficiency" is in principle perfect and a parameter-independent improvement in fidelity of about 2 orders of magnitude is numerically demonstrated. This design can further be generalized to any multiply controlled-X ($\mathrm{C}^n\mathrm{X}$) gate with no additional multiqubit interactions. The residual phase errors with this design are due to second-order effects that cause imperfections in the applied feedback.

C. Locally flat Hamiltonian

This third method is the first of a second strategy, which consists in minimizing the amount of computational information transferred from the memory to the buffer mode by the gate process. In doing so, the environment cannot in turn receive information by measuring buffer output photons, so qubit coherence is preserved. This gate design is presented in Sec. VII. It introduces drive Hamiltonians of the form $\mathbf{H} = f(\mathbf{x})$, where $\mathbf{x} = \mathbf{a} + \mathbf{a}^\dagger$ is the real field quadrature operator on the cat-qubit mode and such that $f(x)$ describes a quasipotential that is locally flat around $x = \pm\alpha$ but with different mean values $f(\alpha) \neq f(-\alpha)$. The first condition ensures that the drive Hamiltonian is approximately constant over the $\mathbf{x}$ eigenstates spanned by each computational state $|\pm\alpha\rangle$, such that it induces almost no dynamics on them and they stay inside the code space throughout the gate. The second condition ensures that each computational state picks up a different phase and hence a rotation about the Z axis. Such Hamiltonians can be engineered with various orders of odd polynomials in $\mathbf{x}$ and, in the limit of a polynomial of infinite order, $f(x)$ would essentially become the sign function; then exponentially low gate errors in $|\alpha|^2$ are demonstrated, only limited by the finite overlap of coherent states $|\alpha\rangle$ and $|-\alpha\rangle$.

D. Discrete jump

Section VIII introduces a cat-qubit gate design based on a tailored "discrete" dissipation. Concretely, through interaction with an ancillary-qubit mode, exactly a single photon is subtracted from the system and the cat state is mapped onto the same state with a gate applied and hence in a discrete manner. Furthermore, for the specific angle $\theta = \pi$, the system stays exactly within its code space during gates, so no information is transmitted to the environment, opening the door to exponentially low gate errors.

The main limitation of this gate design lies in the introduced ancillary qubit. Indeed, ancillary-qubit relaxation

would result in additional $Z(\theta)$ rotations for $Z(\theta)$ gates or additional $Z(\pi)$ rotations for controlled-Z (CZ) gates. In the case of CNOT or Toffoli gates, it would induce X-gate errors, thus killing the error bias. While the dissipator to be engineered for the $Z(\theta)$ and CZ gates is feasible with current state-of-the-art experiments, a viable way to engineer the required CNOT and Toffoli dissipators thus remains to be found.

E. Combined dissipation and two-photon exchange Hamiltonian

Finally, the combined two-photon exchange Hamiltonian and two-photon dissipation method introduced in Ref. [50] can also yield high-fidelity gates. Indeed, due to the additional two-photon exchange Hamiltonian confinement, the effective displacement of the cat-qubit mode during a gate is greatly reduced, such that less information is transmitted to the buffer mode and thus to the environment. This provides a very simple design for gate-error mitigation, especially considering the similarity between this Hamiltonian and the one required for the usual dissipative confinement. This design is not further treated in this paper and we refer the reader to Ref. [50] for more details.

F. Combining designs

As a final remark in this summary, let us note that the gate designs introduced here can be combined together to further improve gate fidelities. As an example, it could be highly favorable to engineer a dissipative cat qubit with the correlated dissipator in $\mathcal{D}[\mathbf{ab}]$, together with a locally flat Hamiltonian to drive gates, plus possibly an optimized activation profile as in Ref. [49]. However, we treat each design separately for clarity.

V. BUFFER PHOTODETECTION WITH CLASSICAL FEEDBACK

A. Design principle

Consider the model of Eq. (2), with a photodetector measuring the output field of the buffer mode. It is governed by a stochastic master equation (SME) that reads [55]

$$d\boldsymbol{\rho} = -i\,[\mathbf{H}_{AB} + \mathbf{H}_Z, \boldsymbol{\rho}]\,dt + \kappa_b \mathcal{D}_\eta[\mathbf{b}]\boldsymbol{\rho}\,dt + \mathcal{J}[\mathbf{b}]\boldsymbol{\rho}\,dN_\eta, \tag{18}$$

where $\mathbf{H}_{AB}$ denotes two-photon exchange between cat and buffer modes, $\mathbf{H}_Z$ is the drive Hamiltonian,

$$\mathcal{D}_\eta[\mathbf{b}]\boldsymbol{\rho} = \mathcal{D}[\mathbf{b}]\boldsymbol{\rho} - \eta(\mathbf{b}\boldsymbol{\rho}\mathbf{b}^\dagger - \langle \mathbf{b}^\dagger\mathbf{b}\rangle\boldsymbol{\rho}) \tag{19}$$

is a corrected dissipation that accounts for the back action of no-detection events, and

$$\mathcal{J}[\mathbf{b}]\boldsymbol{\rho} = \frac{\mathbf{b}\boldsymbol{\rho}\mathbf{b}^\dagger}{\langle \mathbf{b}^\dagger\mathbf{b}\rangle} - \boldsymbol{\rho} \tag{20}$$

is a stochastic jump process that accounts for detection events. Here, $\eta \in [0,1]$ is the detector efficiency and dN_η denotes a stochastic counting process such that it is unity with probability $\langle dN_\eta\rangle = \eta\kappa_b\langle \mathbf{b}^\dagger\mathbf{b}\rangle dt$ and zero otherwise. Like the nonstochastic master equation, the SME of Eq. (18) features the cat-qubit code space with the buffer in vacuum as its only subspace of steady states. If the system steers away from these steady states—a process otherwise known as "code-space leakage," which is induced during gates in particular—then the buffer mode will get populated through the two-photon exchange interaction and it will output photons to the detector through its large damping rate. During this process, the detector may click, depending on the average buffer-mode population and on the detection efficiency.

An alternative explanation for this process is found from the viewpoint of four-wave mixing, as represented in Fig. 2(a). Indeed, during the dynamics, it is possible for one photon of the gate drive and one photon of the cavity (both at frequency ω_a) to be converted into one photon of the buffer (at frequency ω_b) and one photon of the microwave pump (at frequency $2\omega_a - \omega_b$). Since this buffer photon is then emitted to the environment, the cat-qubit cavity is effectively subject to single-photon dissipation events, thus inducing exact parity swaps on the memory.

During a $Z(\theta)$ gate, we thus have the following situation. First, if no buffer photons are detected during the process, the system follows the dynamics of the no-jump deterministic equation, i.e., Eq. (18) with $dN_\eta = 0$. During the gate, modes $\mathbf{a}$ and $\mathbf{b}$ get entangled but after the gate, $\mathbf{b}$ asymptotically relaxes back to vacuum under the no-detection back action. The cat qubit then gets back to a pure state in which its phase information has been perfectly preserved (in addition to the bit value, which is exponentially protected).

Alternatively, one or several buffer photons can be detected during the process. This time, the system also follows the no-detection dynamics, up until the first detection event, at which point it is projected according to $\boldsymbol{\rho} \to \mathbf{b}\boldsymbol{\rho}\mathbf{b}^\dagger$. This corresponds to a phase jump of approximately π, with the exact angle depending on the jump time and gate parameters. This can be roughly understood by recalling the analysis of Sec. III, where for an approximate model and in the absence of a photodetector, we have observed that $\mathbf{b}(t)$ in the Heisenberg picture is proportional to $\boldsymbol{\sigma}_z$. After a detection-induced jump, we can thus perform classical feedback on the qubit to correct for this π phase shift, hence improving the gate fidelities.

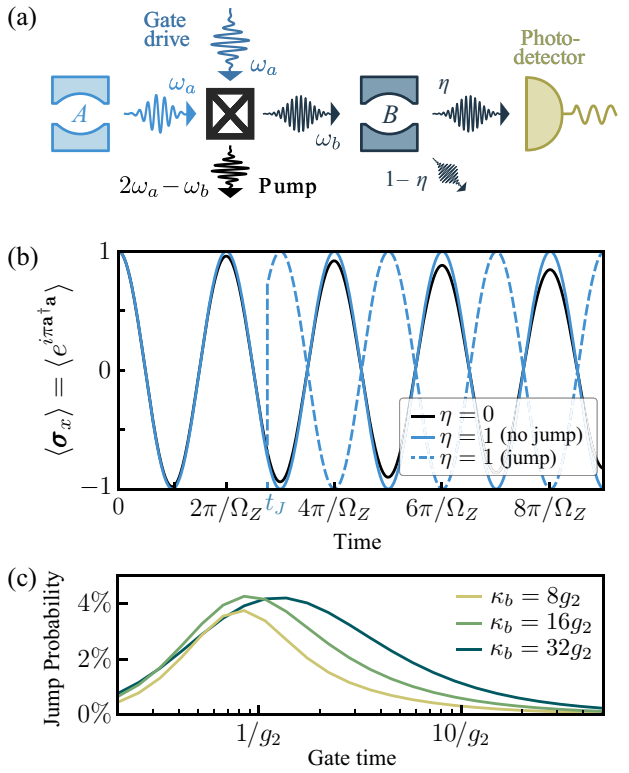

FIG. 2. (a) The four-wave mixing process, showing single cavity photons converted upward into buffer photons when the gate drive is on. They are then measured by a photodetector on the buffer output. (b) Rabi oscillations with a photodetector on the buffer-mode output. The system is initialized in $|+\rangle_L \otimes |0\rangle$ and a constant single-photon drive corresponding to Eq. (6) is turned on at $t = 0$. The parity of the cat-qubit mode is monitored against time for $\eta = 0$ (no detector) and $\eta = 1$ (perfect detector) both for a no-jump trajectory and a single-jump trajectory. In this numerical simulation, $\Omega_Z \equiv 4\alpha\varepsilon_Z = \pi/g_2$, $\kappa_b = 8g_2$ and $|\alpha|^2 = 8$. (c) The total probability of at least one jump occurring during a $Z(\pi)$ gate, for $|\alpha|^2 = 8$.

B. Measurement strategy

The choice of a photodetector on **b**—instead of, e.g., homodyne or heterodyne detection—is motivated as follows. If $\eta = 1$, then no information is lost to the environment and the combined qubit-buffer state remains pure at all times, such that the final cat-qubit state is pure. However, this does not automatically imply that we would be able to perfectly restore the qubit state *before* measurement; indeed, as in a standard perfect measurement, if the detections contain information about the qubit state, then the complementary qubit information is scrambled by back action. According to the analysis of Sec. III, the buffer real quadrature contains information about the qubit being in $|0_L\rangle$ or $|1_L\rangle$ and thus measuring this quadrature would necessarily induce qubit phase decoherence. Therefore, we choose to measure the energy (photon number) of the buffer, which erases this qubit logical information from the detection results and hence should imply preservation of the qubit phase (and bit value) for $\eta = 1$. In other words, by measuring the photon number, we prevent the environment from inducing detrimental back action due to measuring the real quadrature of the buffer.

This picture is in fact exact. Both the Hamiltonian $\mathbf{H}_{AB} + \mathbf{H}_Z$ and the dissipation in $\mathcal{D}[\mathbf{b}]$ commute with a joint x-axis conjugation of both phase spaces. On the output channel **b**, this conjugation involves a minus sign, which a quadrature measurement could in principle detect, but when measuring $\mathbf{b}^\dagger\mathbf{b}$ this sign strictly disappears from the equations. Then the output signal contains zero information about the logical bit value of the cat qubit; hence, for $\eta = 1$, the phase information of the cat qubit must be perfectly preserved. More details on this invariance of the master equation under joint phase conjugation can be found in Appendix D.

C. Jump and no-jump trajectories

Before discussing the full performance of the design with classical feedback, we examine the jump and no-jump trajectories of the scheme separately.

In Fig. 2(a), we show a numerical simulation of Z-axis Rabi oscillations both for a zero-photon-detected trajectory (solid blue) and for a single-photon-detected trajectory (dashed blue), as well as for the standard Zeno gate (black). To evaluate the qubit $\boldsymbol{\sigma}_x$ expectation value when the system is not exactly in code space, we take the photon-number parity of mode **a**. For the standard Zeno design, gate errors accumulate over time, as shown by the decreasing amplitude of oscillations. For the photodetection design, however, the qubit phase converges to an indeterminacy of order 10^{-3} (not visible)—reflecting the steady state entanglement of **a** and **b** modes during gate operation [see Fig. 1(b)]—and then keeps oscillating without loss. The single-jump trajectory clearly shows a full dephasing of angle $\simeq \pi$ after the detection event at a random time $t = t_J$ and, further, keeps oscillating without phase loss. In Fig. 2(b), we show the probability that a detection event will occur during a $Z(\pi)$ gate, as a function of the gate time and assuming an ideal photodetector. This jump probability is evaluated as $p_J = 1 - \exp\big(-\int \langle dN_\eta \rangle(t)\big)$. The low jump probability ensures that trajectories with more than two or three detection events will be extremely rare.

The perfect preservation of the cat-qubit phase by the gate operation holds after full disentanglement of the memory and buffer modes, which includes a reconvergence phase to the cat-qubit code space after the gate drive has been turned off while still monitoring **b** with the photodetector. This is illustrated in Fig. 3(a), for two time-dependent shapes of single-photon drives. For $t \in [0, T]$—i.e., while the gate drive is on—the build-up of a π-angle Rabi oscillation is observed, with better phase

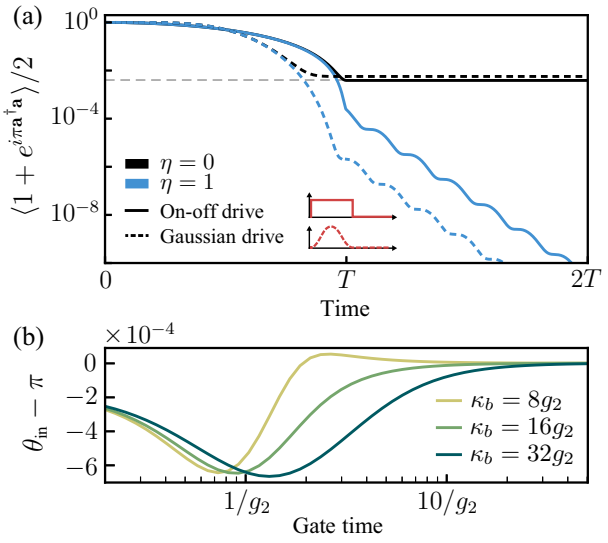

FIG. 3. (a) The time evolution of the parity during a $Z(\pi)$ gate with an ideal photodetector on the buffer-mode output ($\eta = 1$) and without ($\eta = 0$). Only the no-detection trajectory is shown. The system is initialized in $|+\rangle_L \otimes |0\rangle$ and a single-photon drive corresponding to Eq. (6) is on for $0 < t < T$. For $t > T$, the buffer mode reconverges to vacuum as it disentangles from the cat-qubit mode. The dashed gray horizontal line shows Eq. (17). In this numerical simulation, $T = 4/g_2$, $\kappa_b = 8g_2$ and $|\alpha|^2 = 8$. (b) The input angle $\theta_{\text{in}} = 4\alpha \int \varepsilon_Z dt$, such that an exact $Z(\pi)$ gate is produced after an infinite-time reconvergence to the buffer-mode vacuum.

precision in the presence of a photodetector ($\eta = 1$, blue) than without a detector ($\eta = 0$, black). Also, as already observed in Ref. [49], the Gaussian-like time-dependent drive offers significantly better performance because the system mode is closer to its driveless steady state at the end of the gate. For $t > T$, the single-photon drive is turned off and the reconvergence begins. In the absence of a photodetector, the qubit phase remains perfectly constant during reconvergence, since the photon-number parity is conserved by the two-photon dissipation dynamics. This is shown in Fig. 3(a) for the black curves. In contrast, when keeping the photodetector on the **b** mode for $t > T$, the SME does not preserve photon-number parity due to the nonlinear back-action terms featured in Eq. (20) and therefore it is indeed possible to further improve the phase precision as the modes progressively disentangle. The oscillations observed during this reconvergence are due to the damped harmonic oscillator behavior of the mode, as shown in Eq. (16b).

For $\eta = 1$, in principle there is no limit to phase precision after full disentanglement. To check this, we have adjusted the drive amplitude numerically to perform an ideal $Z(\pi)$ gate at $t \to \infty$, as shown in Fig. 3(a). Then, we have checked that the same drive amplitude indeed performs rotations of the same angle whatever the initial cat-qubit state. In Fig. 3(b), we show the typical small correction to be applied on the drive amplitude for trajectories without measurement detections.

D. Design performance

We now describe the performance of the full design with buffer-mode photodetection and classical feedback. To quantify this, we simulate the following master equation,

$$d\boldsymbol{\rho} = -i\,[\mathbf{H}_{AB} + \mathbf{H}_Z, \boldsymbol{\rho}]\,dt + \kappa_b \mathcal{D}_\eta[\mathbf{b}]\boldsymbol{\rho}\,dt + \mathcal{J}[\mathbf{Z}(\pi)\mathbf{b}]\boldsymbol{\rho}\,dN_\eta \qquad (21)$$

which is the same as Eq. (18) but with a jump operator in $\mathbf{Z}(\pi)\mathbf{b}$ that indicates a Pauli correction on the memory mode for every buffer photon detected. Note that this stochastic master equation does not correspond to any physical model. We only introduce it to explain and quantify the idea behind the design. The actual feedback should be applied separately from the photodetection, e.g., in software before any non-Clifford gate or with a subsequent $Z(k\pi)$ gate, where k is the number of detected photons. Alternatively, erasure errors can be included in the model, in which case qubits with at least one buffer photon detected during gates are discarded. Hence, with this plethora of possible feedback strategies, we limit our study to Eq. (21).

The $Z(\pi)$ gate performance achieved after a finite time with this design is shown in Fig. 4(a). The curves result from an average over several realizations for which the photodetector may have clicked at different times and the drive is optimized for the zero-detection trajectory to achieve an ideal gate after full reconvergence to the code space. For this feedback scheme, the gate fidelity is limited by finite detection efficiency, as shown by the linear

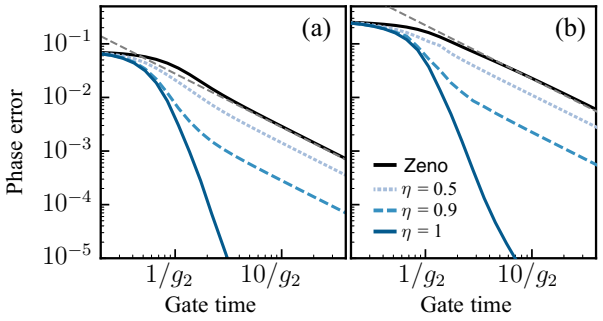

FIG. 4. The phase errors of $Z(\pi)$ and CNOT gates for the standard Zeno design ($\eta = 0$, black) and with a photodetector on the buffer-mode output of the cat qubits (blue). The figure shows an average over every possible stochastic trajectory for the photodetection design of Eq. (21). The gate drives are the Hamiltonians of Eqs. (6) and (9), with Gaussian time dependence. The dashed gray lines show Eqs. (A4) and (A5). In these numerical simulations, $\kappa_b = 8g_2$ and $|\alpha|^2 = 8$.

scaling of dashed blue lines that correspond to $\eta = 0.5$ and $\eta = 0.9$. For the ideal photodetector $\eta = 1$, the gate fidelities scale with a high-order polynomial in the gate time. In principle, working toward ultimate precision, one could perform an ideal feedback of angle $\phi(t_J) \approx \pi$ that depends on the exact jump time and obtain an errorless gate. This is discussed further in Appendix E.

Generalization of the design to multiqubit CNOT and Toffoli gates is quite straightforward. Considering only the simpler scheme of Ref. [50], for which target-mode stabilization is turned off during the gate process, photodetection should be performed on the buffer-mode output of the control qubit(s) only. The numerical performance of this design for the CNOT gate is shown in Fig. 4(b). Here, feedback is also assumed to be perfectly applied following every buffer-mode photodetection, according to Eq. (21). Similarly to the single-qubit gate, we find a fidelity improvement of several orders of magnitude in the ideal photodetector case and otherwise a fidelity improvement limited by the detection efficiency. In Sec. V E, we discuss nonideal photodetectors in more detail.

E. Nonideal photodetector

A realistic photodetector is never ideal and features a finite detection efficiency η. In this case, only part of the information lost to the environment is retrieved and the resulting gate features dynamics in between the two regimes $\eta = 0$ and $\eta = 1$. A lower bound on the error is then given by

$$p_Z \gtrsim (1 - \eta)\, p_Z^{(0)}, \tag{22}$$

where $p_Z^{(0)}$ is the phase error of the regular Zeno gate, e.g., as given by Eq. (17) for the $Z(\theta)$ gate. Indeed, a fraction $(1 - \eta)$ of the state would behave as in the absence of a photodetector. We denote this as approximate because, when the photodetector does click, we can herald a successful detection trajectory if such heralding is compatible with the rest of the architecture.

In Fig. 5, we show the numerical scaling of the phase errors of a $Z(\pi)$ gate against the detection inefficiency $1 - \eta$ in log-log scale. We indeed find a linear scaling with the amount of information lost to the environment according to Eq. (22), which eventually saturates for large enough detection efficiencies. This saturation results from the imperfect reconvergence to the code space, as previously discussed.

In practice, a nonideal photodetector not only features a nonunity detection efficiency but it may also have a finite dark-count rate (the detector clicks without any photon being measured) and a finite uncertainty on the detection time. The former would result in the erroneous application of a π-angle feedback at the dark-count rate similar to thermal photons in the buffer mode (see Appendix C). The latter has no impact on the design fidelity, since a $Z(\pi)$ correction gate should be applied independently of the detection time. In any case, both of these effects are widely negligible compared to detection inefficiency, which even with state-of-the-art photodetectors is typically in the $\eta = 0.1$–0.5 range. With the rapid improvement in photodetector efficiencies [56–58], we may, however, expect this gate design to become viable in the coming years [see also Fig. 13(a)]. The design can also inspire other feedback methods in which feedback is hardware efficient or made autonomously, such as the one introduced in Sec. VI.

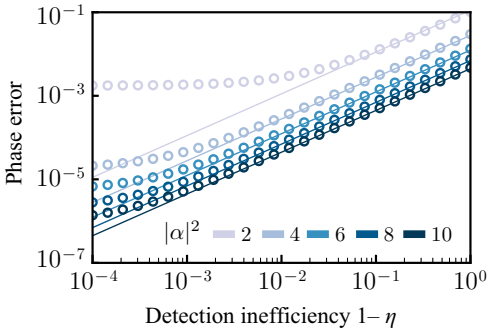

FIG. 5. Scaling of the phase errors of a $Z(\pi)$ gate against the detection inefficiency $1 - \eta$, for increasing values of $|\alpha|^2$. The gate errors are evaluated at $t = T = 4/g_2$, without reconvergence ($T_c = 0$). The markers show numerical integration of the SME with classical feedback. The solid lines show Eq. (22), with a linear scaling with $1 - \eta$. In this numerical simulation, $\kappa_b = 8g_2$.

VI. CAT-BUFFER AUTONOMOUS FEEDBACK

A. Design principle

This second gate design, inspired by the previous one, introduces a correlated dissipator to remove entropy from the system instead of the standard single-photon dissipation on the buffer mode. The corresponding master equation to be engineered on the cavity-buffer system then reads

$$\frac{d\boldsymbol{\rho}}{dt} = -i\,[\mathbf{H}_{AB} + \mathbf{H}_Z, \boldsymbol{\rho}] + \kappa_{ab}\mathcal{D}[\mathbf{ab}]\boldsymbol{\rho}, \tag{23}$$

with the main addition of a two-mode dissipation operator that was recently realized in Ref. [59] in the context of pair–cat-code stabilization [22]. The main idea behind this peculiar dissipation arises from the photodetector scheme of the previous section. When the cat-qubit leaks out of its code space under the gate drive, the buffer mode is populated through the $\mathbf{H}_{AB}$ interaction, then inducing an eventual phase flip on the cavity mode as explained in Sec. III. The correlated dissipation thus ensures that whenever the buffer mode loses a photon (hence inducing a $Z(\pi)$ error on the logical cat qubit), a direct photon loss

on the cavity mode is also produced, thus switching the cat-qubit parity a second time and correcting for the error autonomously.

Mathematically, this can be understood using the shifted Fock-basis [37] transformation as defined in Eq. (11), which yields

$$\kappa_{ab}\mathcal{D}[\mathbf{ab}] \to \kappa_{ab}\mathcal{D}[\boldsymbol{\sigma}_z(\tilde{\mathbf{a}}+\alpha)\mathbf{b}] = |\alpha|^2\kappa_{ab}\mathcal{D}[\boldsymbol{\sigma}_z\mathbf{b}] + \mathcal{O}\left(|\tilde{\mathbf{a}}^\dagger\tilde{\mathbf{a}}|^{1/2}\right), \tag{24}$$

where the second-line approximation holds since $|\tilde{\mathbf{a}}^\dagger\tilde{\mathbf{a}}| \ll 1$ in the limit of a small amount of leakage. Keeping only the leading-order term in Eq. (24) and taking $\kappa_b \equiv |\alpha|^2\kappa_{ab}$, it is possible to perform the same gate-error derivation as in Sec. III. This yields the exact same resulting set of equations on $\mathbf{a}$ and $\mathbf{b}$ but with a different dissipation operator in $\boldsymbol{\sigma}_z\mathbf{b} \propto \boldsymbol{\sigma}_z^2 = \mathbf{I}$, where $\mathbf{I}$ is the identity on the two-level cat-qubit mode; i.e., the environment does not receive any information about the qubit state, as required. We emphasize once again that this derivation is only first order and that nonlinear effects have been neglected, e.g., with terms in $\tilde{\mathbf{a}}^2\mathbf{b}^\dagger + \text{h.c.}$ that may eventually limit the gate performance.

To engineer the correlated dissipation of Eq. (23), an ancillary low-Q reservoir mode $\mathbf{r}$ can be introduced into the setup [59]. By engineering four-wave mixing between those three modes and a classical pump, it is then possible to enable Hamiltonian interaction of the form $g_{ab}\mathbf{abr}^\dagger + g_{ab}^*\mathbf{a}^\dagger\mathbf{b}^\dagger\mathbf{r}$. Together with a large reservoir damping of the form $\kappa_r\mathcal{D}[\mathbf{r}]$ and in the limit of $\kappa_r \gg g_{ab}$, it is possible to eliminate the fast dynamics of the reservoir mode. In the reduced system of the cat and buffer modes, the required correlated dissipator is then obtained, with typical amplitude $\kappa_{ab} = 4g_{ab}^2/\kappa_r$ [52].

In addition, preparing pure cat states from the memory-mode vacuum using the correlated dissipation of Eq. (23) cannot be achieved by simply driving the buffer mode, as would be done with a standard two-photon dissipation setup. Indeed, the parity-switching dissipation would instead prepare a statistical mixture of coherent states $|\pm\alpha\rangle$ by leaking out parity information to the environment. As such, state preparation can be achieved in one of two ways. The first possibility is to momentarily switch to a standard two-photon dissipation setup, by engineering a four-wave mixing term in $g_{2,r}(\mathbf{a}^2-\alpha^2)\mathbf{r}^\dagger + \text{h.c.}$ while turning off the other four-wave mixing terms that involve the buffer mode. Alternatively, one can keep the correlated dissipation on at all times and adiabatically turn on the buffer drive. Indeed, parity is then preserved, since the buffer mode is only populated to second order in the drive amplitude.

In the limit of $\kappa_{ab}|\alpha|^2 \gg g_2$, it is further possible to eliminate the fast dynamics of the buffer mode to obtain an effective single-mode master equation on the cat qubit. Use of the effective-operator formalism of Ref. [60] yields the following dynamics on the cat-qubit mode,

$$\frac{d\boldsymbol{\rho}}{dt} = \frac{4g_2^2}{\kappa_{ab}}\mathcal{D}\left[\mathbf{a}(\mathbf{a}^\dagger\mathbf{a})^{-1}(\mathbf{a}^2-\alpha^2)\right]\boldsymbol{\rho}, \tag{25}$$

where $(\mathbf{a}^\dagger\mathbf{a})^{-1}$ is the pseudoinverse of the photon-number operator and describes the effective difference in the dynamics undergone during transient buffer excitation. This master equation indeed describes a parity-switching stabilization of the cat mode but it differs from the master equation targeted in Ref. [51]. More details on this model reduction can be found in Appendix F.

B. Parity-switching dynamics

This dissipation with $\mathcal{D}[\mathbf{ab}]$ is activated more generally when the cat-qubit leaks out of its code space, triggering a reaction of its buffer. The effect will be beneficial whenever the leakage source is associated with parity switching. For standard cat qubits, this is mainly the case for the user-induced Zeno dynamics as just discussed (for $Z(\theta)$ gates, on the control qubit of CNOT gates, or other similar gates). It can also occur by thermal excitation of the cat mode, of the form $\mathcal{D}[\mathbf{a}^\dagger]$. In contrast, leakage that preserves the photon-number parity would then induce phase errors by following the same process. For example, this is true of pure dephasing of the form $\mathcal{D}[\mathbf{a}^\dagger\mathbf{a}]$. However, the amplitude of such effects is often negligible compared to other sources of phase errors, such as gates and finite resonator lifetime.

Reference [51] also explores how single-photon losses, of the form $\mathcal{D}[\mathbf{a}]$, can induce parity-switching leakage on a squeezed cat qubit. Indeed, while the annihilation operator leaves the coherent states constituting regular cats in place, it induces leakage on squeezed coherent states [26]. As such, similarly to Ref. [51], the correlated dissipator introduced in this work performs an autonomous correction of single-photon annihilation on squeezed cats, to first order; a better correction would be obtained with dissipation in $\mathcal{D}[S(\mathbf{a})\mathbf{b}]$, where $S(\mathbf{a})$ is the squeezed annihilation operator, featuring the squeezed coherent state as an eigenstate.

One of the main limitations of such approaches stems from thermal noise in the buffer mode, since any buffer excitation would decay by triggering a phase flip on the cat qubit. This effect is further discussed in Appendix C.

C. Design performance

Let us now focus on the performance of this gate design, starting with the single-qubit $Z(\theta)$ gate. In Fig. 6, we show the errors induced by a $Z(\theta)$ gate for the regular Zeno gate (black) and for the correlated-dissipator design of Eq. (23) (blue) for both phase-flip and bit-flip errors. Following our previous analysis, the comparison between the two designs is made at fixed $\kappa_b = |\alpha|^2\kappa_{ab} = 8g_2$ in order to keep the

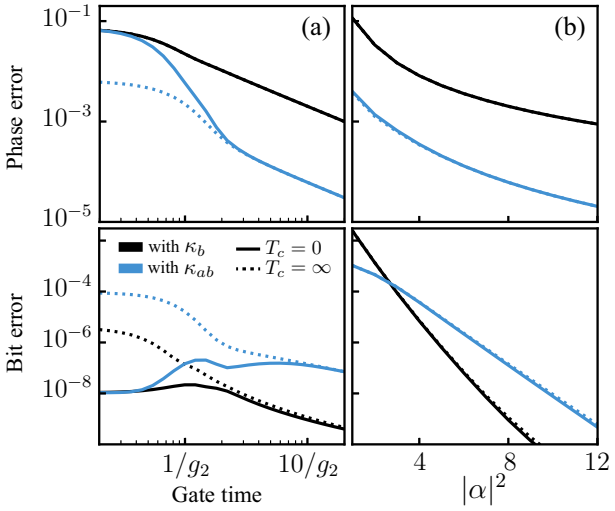

FIG. 6. The gate errors of a $Z(\pi)$ gate with the autonomous-feedback design of Eq. (23) at $\kappa_{ab}/|\alpha|^2 = 8g_2$ (blue) and with the regular Zeno design at $\kappa_b = 8g_2$ (black): (a) fixed cat size, $|\alpha|^2 = 8$; (b) fixed gate time, $T = 10/g_2$. The gate errors are evaluated at $t = T$ or after full reconvergence to the steady state ($T_c = \infty$). While the cat qubit is entangled with its buffer and leaks out of the code space, the logical phase value is evaluated with photon-number parity on **a** and the logical bit value is evaluated with two-photon dissipation invariant [30].

same damping rate. The left-hand-side plots show the scaling with the gate time, while the right-hand-side is plotted against the cat size. For phase-flip errors, an improvement by a constant factor of about $\mu \approx 0.02$ is found, independent of both the gate time and the cat size and limited by second-order effects as discussed previously. In the regime of short gate times, the gate drive is large in amplitude and so the buffer is largely entangled with the cat mode at the end of the gate. For this reason, a reconvergence time is required to reach the constant fidelity gain of μ. In other words, the buffer has not had enough time to lose its excitations to the environment and so the correlated dissipator has not yet corrected for the coherent errors that occurred during the gate.

The correlated dissipator of Eq. (23) can raise concerns about bit-flip errors since it would, by itself, stabilize the vacuum state in both resonators. Hence, the bottom plots of Fig. 6 investigate this bit-flip error and show that the exponential scaling in $|\alpha|^2$ is preserved, although slightly degraded from that of the regular Zeno gate. This is likely due to the additional leakage induced by the correlated dissipator. Indeed, whenever the buffer mode is populated, the cat mode is pushed toward its own vacuum state, at a rate proportional to the buffer population. When stopping operation before reconvergence (solid blue curve), the bit-flip rate looks artificially reduced for very short gate times, as the buffer has not yet had time to dissipate.

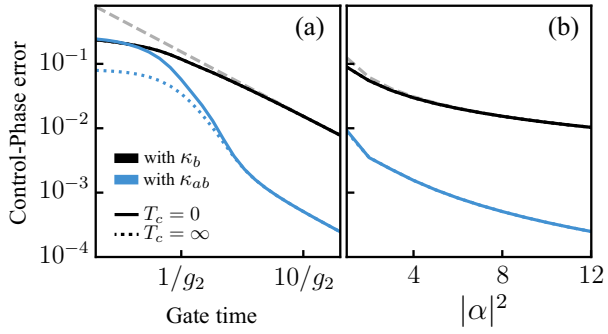

FIG. 7. The gate errors of a CNOT gate with the autonomous-feedback design of Eq. (23) at $\kappa_{ab}/|\alpha|^2 = 8g_2$ (blue) and with the regular Zeno design at $\kappa_b = 8g_2$ (black): (a) fixed cat size, $|\alpha|^2 = 8$; (b) fixed gate time, $T = 10/g_2$. The gate errors are evaluated at $t = T$ or after full reconvergence to the steady state ($T_c = \infty$). The dashed gray lines show Eq. (A5).

D. Multiqubit gates

For CNOT and Toffoli gates, the gate drive is parity preserving on the target qubit. As explained for the buffer-photodetection gate design, in principle, then detecting all buffer relaxations would induce a combination of phase corrections on the control qubit; to first order, however, this comes down to only requiring the correlated dissipation on control qubits. In Fig. 7, we investigate the performance of such a setup for two-qubit CNOT gates. The correlated dissipator of Eq. (23) is activated on the control qubit and the drive Hamiltonian of Eq. (9) is switched on. Here, the performance is very similar to that of the single-qubit $Z(\theta)$ gate, with a phase fidelity improvement of $1/\mu \approx 50$ in the best-case scenario. This is obtained at large gate times when the drive is small compared to the damping rate, $\varepsilon_{CX} \ll \kappa_{ab}|\alpha|^2$.

VII. LOCALLY FLAT HAMILTONIAN

A. Intuition

Quantum states feature a dispersion in position and momentum in their phase-space representation, with an equal variance in the case of coherent states. A single-photon drive, such as the gate drive of Eq. (6), thus acts differently along this dispersion and according to the specific position and momentum values of the state. This induces a phase-space displacement that can be frozen by a continuous measurement, such as the one of two-photon dissipation. This is the so-called Zeno effect.

From the wave-function perspective, a coherent state is Gaussian in position representation [61] and, for a real coherent amplitude, reads $\psi(x) \propto \exp\left[-(x - \langle x\rangle)^2/2\right]$. Since the Zeno drive of Eq. (6) reads $H_Z(x) = \varepsilon_Z x$ in this same representation, the time evolution of the wave function under H_Z can be trivially obtained, as after some time t, the wave function reads $\psi(x,t) \propto \exp[-ix\varepsilon_Z t]\psi(x)$.

This corresponds to a position-dependent phase shift and therefore a displacement along the momentum axis p. However, two-photon dissipation prevents this displacement and only the average phase shift $\exp[-i\langle x\rangle\varepsilon_Z t]$ remains, thus driving a cat-qubit $Z(\theta)$ gate together with a logical phase blurring reflecting the variance of $\exp[-ix\varepsilon_Z t]$ over each coherent state.

From this viewpoint, one way to improve the precision of the $Z(\theta)$ gate is to use a drive Hamiltonian with little dispersion over each coherent state. Moreover, this property should be robust to all effects that the cat qubit is meant to cover, i.e., most prominently, local displacements in phase space. Conversely, such a Hamiltonian would induce almost no displacement of the coherent states, nor deformation of any kind. Hence the phase gate could be implemented without relying on two-photon dissipation and the evolution can be purely unitary, which is another way to see that the gate would induce no phase losses.

B. Design principle

In this sense, an ideal [62] drive Hamiltonian for single-qubit $Z(\theta)$ gates reads

$$\mathbf{H}_{Z,\infty} \equiv \varepsilon_Z \,\mathrm{sign}(\mathbf{x}), \tag{26}$$

where "sign" denotes the sign function and $\mathbf{x} = \mathbf{a} + \mathbf{a}^\dagger$. This Hamiltonian yields a global phase difference for each half-plane of phase space and thus engineers the required gate without any phase loss while being robust to any local error—e.g., small displacements or distortions of cat states. It is represented by thin black lines in Fig. 8(a), together with the position representation of a superposition cat state in the background. In Figs 8(b) and 8(c), we show the phase errors induced by such a single-qubit $Z(\pi)$ gate with the Hamiltonian of Eq. (26) shown by black lines, both for varying gate time (left) and varying cat size (right). We indeed find that this Hamiltonian provides phase errors that scale exponentially in the cat size and that are drastically smaller than with the regular Zeno Hamiltonian of Eq. (6), represented using blue lines.

The Hamiltonian of Eq. (26) is highly nonlinear in $\mathbf{x}$ and is therefore not accessible for state-of-the-art superconducting circuits, nor for other quantum computation platforms. It can, however, be approximated. Let us define the set of Hamiltonians

$$\mathbf{H}_{Z,N} \equiv \varepsilon_Z \sum_{n=0}^{N} c_n \mathbf{x}^{2n+1} \tag{27}$$

for $N \geq 0$, where the c_n are constants to be determined. These Hamiltonians have an odd distribution in position space. With the proper definition of c_n, they can approximate the sign Hamiltonian of Eq. (26) locally around each cat-qubit coherent state, even if the approximation

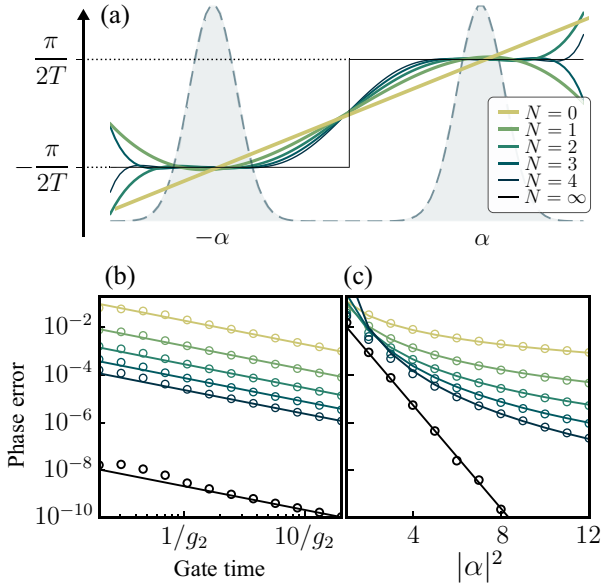

FIG. 8. (a) The position distribution of locally flat drive Hamiltonians of Eqs. (26) and (27) that minimize the variance over the quantum fluctuations of cat states. (b),(c) The gate phase errors for a $Z(\pi)$ gate with a locally flat drive Hamiltonian at (b) fixed cat size, $|\alpha|^2 = 8$, and (c) fixed gate time, $T = 10/g_2$. In these simulations, $\kappa_b = 8g_2$. The lines show numerical fits of the form $p_Z \propto T^{-1}|\alpha|^{-2(2+N)}$ (color) and $p_Z \propto T^{-1}\exp(-2|\alpha|^2)$ (black). The markers show numerical data.

cannot be global. The optimal c_n constants should therefore minimize the gate errors induced by the combination of two-photon dissipation and drive during a given gate. Loosely speaking, these errors scale with the amount of nonflatness of the drive Hamiltonian of Eq. (27)—a perfectly flat drive Hamiltonian would not displace the state and would thus result in an error-free gate. Therefore, we minimize the variance of the Hamiltonian across a single coherent state, given by

$$V_N(\{c_n\}) \equiv \frac{1}{\sqrt{2\pi}} \int_{-\infty}^{\infty} H_{Z,N}(x)^2 \mathrm{e}^{-\frac{1}{2}(x-2\alpha)^2} dx, \tag{28}$$

under the constraint of a fixed angle of gate rotation,

$$\frac{1}{\sqrt{2\pi}} \int_{-\infty}^{\infty} H_{Z,N}(x) \mathrm{e}^{-\frac{1}{2}(x-2\alpha)^2} dx = \frac{\theta}{2T}, \tag{29}$$

where $H_{Z,N}(x)$ is the position distribution of the Hamiltonian of Eq. (27). This optimization problem is solved numerically using a Lagrange multiplier, which is differentiated analytically and then minimized through matrix inversion. More details on this minimization can be found in Appendix G.

In Fig. 8(a), we show the first five of these Hamiltonians using colored lines, as determined by the previously described minimization process. While $N = 0$ corresponds

to the regular Zeno Hamiltonian of Eq. (6) with a linear distribution, the $N > 0$ Hamiltonians show locally flat distributions around both coherent states, with increasing flatness as N grows.

C. Results

The performance of these Hamiltonians is then evaluated for the single-qubit $Z(\pi)$ gate in Figs. 8(b) and 8(c), with the gate phase error as a function of the gate time and the cat size, respectively. The first plot shows a constant improvement in phase fidelity of the gate as N increases, while the scaling with the gate time stays linear. The second plot, however, shows an improved scaling of phase errors with the cat size as N grows. Although we lack an analytical derivation of phase errors for this set of drive Hamiltonians, a numerical fit of the form $p_Z \propto |\alpha|^{-2(2+N)}$ is performed as highlighted by the colored lines and it matches the numerical simulations particularly well in the large-cat-size limit. We attribute this scaling to the fact that, as both coherent states come further apart in phase space, the variance-minimization process can achieve flatter distributions with each additional degree of freedom provided by the increasing N.

D. Multiqubit gates

Generalization of this single-qubit gate design to multiqubit gates is quite straightforward. Similarly as for the regular Zeno gate, the single-qubit drive of Eq. (27) should be multiplied by a phase-space rotation on the target qubit, which yields

$$\mathbf{H}_{\mathrm{CX},N} \equiv \varepsilon_{\mathrm{CX}} \left(\sum_{n=0}^{N} c_n \mathbf{x}_C^{2n+1} \right) \otimes \left(\mathbf{a}_T^\dagger \mathbf{a}_T - n_p \right), \tag{30}$$

where $\mathbf{x}_C = \mathbf{a}_C + \mathbf{a}_C^\dagger$, the $\mathbf{a}_{C/T}$ are annihilation operators on the control and target qubits, respectively, and n_p is any even integer close to $|\alpha|^2$. Together with a static two-photon dissipation on the control qubit and optionally with the correlated two-photon dissipation on the target qubit [36], this process achieves a CNOT gate.

In Fig. 9, we investigate the phase errors induced by this two-qubit gate design on the control qubit, both against the gate time (left) and the cat size (right). Similar conclusions as for the single-qubit $Z(\theta)$ gate are reached. The gate errors scale linearly with time and numerically we fit these errors according to $p_{Z_C} \propto |\alpha|^{-2(1+N)}$. The $|\alpha|^2$ difference in scaling compared to the single-qubit gate is due to the target-qubit term in the drive Hamiltonian of Eq. (30). Indeed, the operator $\mathbf{a}_T^\dagger \mathbf{a}_T - n_p$ induces a different (integer) number of $Z(\pi)$ gates on the control qubit for each Fock state of the target qubit and the dispersion on this number increases with α (for details, see Ref. [37]).

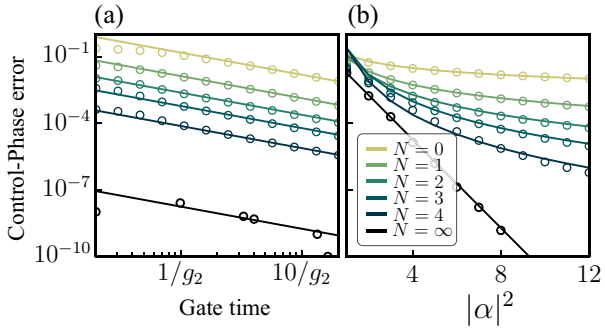

FIG. 9. The gate-induced control-phase errors for a CNOT gate with a locally flat drive Hamiltonian as in Eq. (30): (a) fixed cat size, $|\alpha|^2 = 8$; (b) fixed gate time $T = 10/g_2$. Dissipative stabilization is acting on the control qubit only, with $\kappa_b = 8g_2$. The lines show numerical fits of the form $p_{Z_C} \propto T^{-1}|\alpha|^{-2N}$ (color) and $p_{Z_C} \propto T^{-1}\exp(-2|\alpha|^2)$ (black). The markers show numerical data.

E. Engineering with an ATS

Overall, the high-order Hamiltonians introduced in this section can greatly improve the performance of dissipative cat-qubit gates, at the cost of additional difficulties in engineering the required Hamiltonians. Let us note, however, that high-order nonlinearities are always present in superconducting circuits, even if they are often neglected due to their low amplitudes. Since the c_n coefficients scale as $c_n \propto |\alpha|^{-2n}$, even moderate superconducting nonlinearities could be enough to engineer these Hamiltonians and especially so in the large-cat-size limit.

To illustrate this possibility, let us consider a realistic set of parameters for the current experimental proposal of dissipative cat qubits based on the asymmetrically threaded superconducting quantum interference device (SQUID), i.e., the ATS [42,43]. The ATS is a nonlinear circuit element made of a SQUID shunted by an inductance, which creates two flux loops that are then threaded at 0 and π flux bias, respectively. The ideal Hamiltonian resulting from this setup reads

$$\mathbf{H} = \omega_a \mathbf{a}^\dagger \mathbf{a} + \omega_b \mathbf{b}^\dagger \mathbf{b} - 2E_J \varepsilon(t) \sin\left(\varphi_a(\mathbf{a} + \mathbf{a}^\dagger) + \varphi_b(\mathbf{b} + \mathbf{b}^\dagger)\right) \tag{31}$$

for an ATS coupled capacitively to both the cat-qubit and buffer modes. Here, the $\varepsilon(t)$ term corresponds to a differential flux drive that can be frequency tuned to make specific terms in the sine Hamiltonian resonant. Also, $\varphi_{a/b}$ denote the energy participation of each mode into the ATS. Typically, it is desired to engineer φ_a as large as possible to create strong two-to-one photon exchange rates, bearing in mind that a large φ_a also induces increased high-order nonlinear effects and increased single-photon losses by coupling to the buffer transmission line.

For concreteness, let us assume that we want to implement a $Z(\pi)$ gate as in Eq. (27) with $N = 2$ (i.e., up to fifth-order Hamiltonian terms), with a gate time $T = 500$ ns and for a cat of size $|\alpha|^2 = 8$. In this case, the global-drive-Hamiltonian amplitude to be engineered reads $\varepsilon_Z/2\pi = 1/8\alpha T \approx 88$ KHz and the polynomial coefficients of order 1, 3, and 5 read $c_0 \approx 0.66$, $c_1 \approx -0.055$ and $c_2 \approx 0.0021$, respectively. To make each of these coefficients match the ATS Hamiltonian terms, the following identities should be met:

$$\varepsilon_Z c_0 = 2E_J \varepsilon_0 \varphi_a + \mathcal{O}(\varphi_a^3), \tag{32a}$$

$$\varepsilon_Z c_1 = 2E_J \varepsilon_1 \varphi_a^3/3! + \mathcal{O}(\varphi_a^5), \tag{32b}$$

$$\varepsilon_Z c_2 = 2E_J \varepsilon_2 \varphi_a^5/5! + \mathcal{O}(\varphi_a^7), \tag{32c}$$

where $\varepsilon_k \ll 1$ are the flux drive amplitudes such that $\varepsilon(t) = \sum_k \varepsilon_k \cos((2k+1)\omega_a t)$. The right-hand-side terms simply result from a Taylor expansion of the sine up to fifth order in $\varphi_{a/b} \ll 1$. Further assuming realistic experimental parameters of $\varepsilon_k = 0.01$, $\varphi_a = 0.1$, and $E_J/2\pi = 90$ GHz [42], we find that the right-hand-side terms of Eq. (32) are at least 10 times larger than required by the left-hand-side terms. In other words, the achievable experimental parameters are 10 times larger than the actual drive amplitudes to be engineered. This gives some leeway to either implement even higher-order gate designs or to release experimental constraints. In addition, for the same parameters, a factor of $|\alpha|^4 = 64$ improvement in gate fidelities can be expected, making the design particularly attractive.

As a final remark, one may also seek to engineer such nonlinear terms, e.g., with time-dependent schemes and the rotating-wave approximation or by involving auxiliary systems. However, during such attempts, one should keep in mind the utmost importance of preserving the noise bias throughout gate operation.

VIII. DISCRETE JUMP

For this final design, we shift away from the Zeno effect that has up to now been the common basis for all physical cat gate implementations with a Z component. This section introduces discrete gates that rely on a dissipative coupling to an ancillary mode. We begin with single-qubit $Z(\theta)$ gates and generalize to CZ and CNOT gates afterward.

A. Design principle

Consider the following master equation with the buffer mode adiabatically eliminated:

$$\frac{d\boldsymbol{\rho}}{dt} = \kappa_2 \mathcal{D}[\mathbf{a}^2 - \alpha^2]\boldsymbol{\rho} + \kappa_Z \mathcal{D}[\mathbf{a}_\theta \boldsymbol{\sigma}_+]\boldsymbol{\rho}, \tag{33}$$

where $\boldsymbol{\sigma}_+$ denotes the creation operator of an ancillary-qubit mode and

$$\mathbf{a}_\theta = \cos(\theta/2)\alpha + i\sin(\theta/2)\mathbf{a} \tag{34}$$

is a modified annihilation operator such that $\mathbf{a}_\pi = i\mathbf{a}$ and $\mathbf{a}_\theta |\pm\alpha\rangle = \exp(\pm i\theta/2)|\pm\alpha\rangle$. From this identity, it is immediate to verify that projecting any cat-qubit state with $\mathbf{a}_\theta$ achieves a $Z(\theta)$ rotation of this state, up to exponentially small corrections in $|\alpha|^2$ to account for state normalization. Furthermore, assuming that this ancillary mode is initialized in its ground state $|g\rangle$ and does not suffer from errors, the correlated dissipator in $\mathbf{a}_\theta \boldsymbol{\sigma}_+$ engineers the loss of exactly one $\mathbf{a}_\theta$ photon from the cat mode, after which nothing more can happen with this dissipation. This can thus be seen as a kind of photon-blockade technique, which can further be made error resilient by, e.g., sending the additional photon to the metastable level of a three-level Λ-system or into an infinite transmission line.

For the particular value $\theta = \pi$, Eq. (33) induces the loss of exactly one $\mathbf{a}$ photon. Since the logical $|\pm_L\rangle$ cat states feature even and odd photon-number parities, respectively, and the logical bit value is exponentially protected under such losses due to the two-photon dissipation, this peculiar dissipator results in a Pauli-$Z(\pi)$ gate on the cat-qubit mode after infinite time evolution.

To estimate gate fidelities at finite times analytically, let us assume that the complete system is initialized in $\boldsymbol{\rho}(0) = \boldsymbol{\rho}_{A,0} \otimes |g\rangle\langle g|$, where $\boldsymbol{\rho}_{A,0}$ is the initial density matrix on the cat mode. The full system density matrix at time t can then be separated along the diagonal matrix elements of the ancillary mode according to $\boldsymbol{\rho} = \boldsymbol{\rho}_g \otimes |g\rangle\langle g| + \boldsymbol{\rho}_e \otimes |e\rangle\langle e|$ (the correlated dissipator of Eq. (33) does not induce diagonal to off-diagonal transitions). Inserting this expression in Eq. (33) thus yields

$$\frac{d\boldsymbol{\rho}_g}{dt} = \kappa_2 \mathcal{D}[\mathbf{a}^2 - \alpha^2]\boldsymbol{\rho}_g - \frac{1}{2}\kappa_Z \left\{\mathbf{a}_\theta^\dagger \mathbf{a}_\theta, \boldsymbol{\rho}_g\right\}, \tag{35a}$$

$$\frac{d\boldsymbol{\rho}_e}{dt} = \kappa_2 \mathcal{D}[\mathbf{a}^2 - \alpha^2]\boldsymbol{\rho}_e + \kappa_Z \mathbf{a}_\theta \boldsymbol{\rho}_g \mathbf{a}_\theta^\dagger, \tag{35b}$$

where $\boldsymbol{\rho}_g(0) = \boldsymbol{\rho}_{A,0}$ and $\boldsymbol{\rho}_e(0) = 0$. Let us first discuss these coupled equations without the $\{\mathbf{a}_\theta^\dagger \mathbf{a}_\theta, \cdot\}$ term of Eq. (35a), which will be shown to be the main limitation of the design. As can be seen from the right-hand-side term in Eq. (35b), a transfer of population is made from $|g\rangle$ to $|e\rangle$ at rate $\kappa_Z|\alpha|^2$. Upon this population transfer, a single $\mathbf{a}_\theta$ projection of the cat mode is performed due to the $\mathbf{a}_\theta \boldsymbol{\rho}_g \mathbf{a}_\theta^\dagger$ term, thus achieving the required gate. The minimal gate-induced phase errors that can be achieved at finite time thus come down to the fraction of states that have not undergone the jump from $|g\rangle$ to $|e\rangle$ and read

$$p_Z = \exp\left(-|\alpha|^2 \kappa_Z t\right), \tag{36}$$

where t is the evolution time under the correlated dissipator. The phase error would thus decrease exponentially with $|\alpha|^2$ and with the effective gate time $\kappa_Z t$.

Let us now consider the effect of the right-hand-side term of Eq. (35a).

For the particular case $\theta = \pi$, since $\mathbf{a}_\pi = i\mathbf{a}$ and thus $\mathbf{a}_\pi^\dagger \mathbf{a}_\pi = \mathbf{a}^\dagger \mathbf{a}$, this term remains a parity-preserving operator. Therefore, the evolution with Eqs. (35a) and (35b) perfectly preserves the phase of the logical qubit, up to inducing the desired phase-flip gate from ρ_g to ρ_e. Besides this, the last term of Eq. (35a) acts much like a dispersive dissipation $\mathcal{D}[\mathbf{a}^\dagger \mathbf{a}]$, inducing noisy rotation of the cat qubit out of its code space. As long as $\alpha\kappa_Z \ll 4|\alpha|^2\kappa_2$, this effect is countered by the two-photon dissipation. Since the mean energies of even and odd cats are exponentially close, the induced logical bit flip is exponentially small in $|\alpha|^2$. Up to an upper bound on κ_Z/α, the exponentially scaling phase gate thus indeed holds.

For gate angles $\theta \neq \pi$, to consider the effect of the last term in Eq. (35a) we write out

$$\mathbf{a}_\theta^\dagger \mathbf{a}_\theta = \cos^2(\theta/2)\,|\alpha|^2 + \sin^2(\theta/2)\,\mathbf{a}^\dagger \mathbf{a} - i\sin(\theta)(\mathbf{a}^\dagger - \mathbf{a})/2. \tag{37}$$

The second line of this operator would induce parity-switching leakage from the cat code space and therefore parity errors at a rate proportional to $\sin^2(\theta)$ once brought back to the code space by two-photon dissipation. The gate fidelities obtained from this scheme are still competitive with other gate designs and particularly in the limit of $\kappa_Z \ll \kappa_2$; see the simulation results below. This can be understood as the last term in Eq. (35a) has an effect roughly similar to a Hamiltonian in $i\sin(\theta)(\mathbf{a}^\dagger - \mathbf{a})$. Hence, much like the analysis of Sec. III, it induces phase errors at a rate proportional to κ_Z^2/κ_2, while the phase gate happens at rate κ_Z.

B. Qutrit design

But in fact, we can do better and retrieve, for any θ, the same performance as the $\theta = \pi$ case, with a slightly more involved gate design. Consider the following master equation:

$$\frac{d\boldsymbol{\rho}}{dt} = \kappa_2 \mathcal{D}[\mathbf{a}^2 - \alpha^2]\boldsymbol{\rho} + \kappa_Z \mathcal{D}[\mathbf{a}_\theta |e\rangle\langle g|] + \kappa_Z \mathcal{D}[\mathbf{a}_{\theta+\pi}|f\rangle\langle g|] + \kappa_Z' \mathcal{D}[\mathbf{a}_\pi |e\rangle\langle f|], \tag{38}$$

where $|g\rangle$, $|e\rangle$, and $|f\rangle$ denote the three lowest energy levels of a qutrit, e.g., that of a transmon. This master equation now involves three population transfers. The first is the same as in Eq. (33) and performs a $Z(\theta)$ gate with a $|g\rangle$ to $|e\rangle$ transfer. The other two terms also describe a $Z(\theta)$ gate but made in two steps by first transferring to $|f\rangle$ and then to $|e\rangle$. The main goal of adding these two terms is to cancel out parity-switching dynamics in the $|g\rangle\langle g|$ subspace. Indeed, we now have that

$$\mathbf{a}_\theta^\dagger \mathbf{a}_\theta + \mathbf{a}_{\theta+\pi}^\dagger \mathbf{a}_{\theta+\pi} \propto \cos^2(\theta/2)|\alpha|^2 + \sin^2(\theta/2)\mathbf{a}^\dagger \mathbf{a}. \tag{39}$$

In the $|f\rangle\langle f|$ subspace, the dynamics are also parity preserving, since a $Z(\pi)$ gate is performed. In other words, two paths have been constructed, both of which feed into the same final state with the required Z rotation angle of θ and the interference of which cancels the parity-switching term in Eq. (37). This scheme would mainly be limited by the qutrit characteristics, to be specified from experimental implementation, and by the requirement that both paths should feature the same rate of dissipation. In the following, we focus on the qubit-enabled $Z(\pi)$ gate and also compare qubit- and qutrit-enabled $Z(\theta)$ gate designs.

C. Results

First, we investigate $Z(\pi)$ gates. In Fig. 10, we show the phase errors induced by this discrete $Z(\pi)$ gate without any additional error processes on the cat or ancillary modes. In Fig. 10(a), the phase errors are shown in semilog scale as a function of time for varying κ_Z/κ_2 and fixed $|\alpha|^2 = 4$ or 8 in the master Eq. (33). For each value of κ_Z/κ_2, both numerical simulations (solid) and the minimal gate-error formula of Eq. (36) (dashed) are shown. We retrieve that, in the limit of $\kappa_Z \ll \kappa_2$, the expected

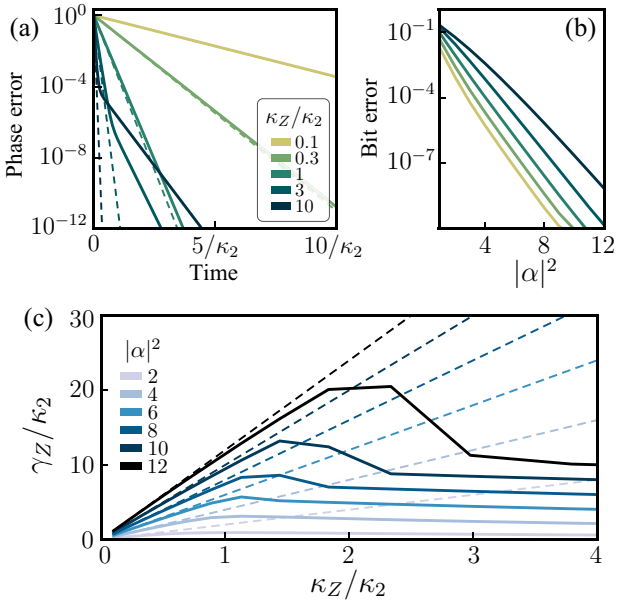

FIG. 10. (a),(b) The gate-induced (a) phase and (b) bit errors of a discrete $Z(\pi)$ gate as in Eq. (33) for multiple values of κ_Z/κ_2: (a) fixed cat size, $|\alpha|^2 = 8$; (b) fixed gate time, $T = 10/\kappa_2$. In (a), the dashed lines show $p_Z = \exp(-|\alpha|^2\kappa_Z t)$. (c) The exponential rate γ_Z obtained from a linear fit of $\gamma(t) = -\ln(p_Z(t)) \propto \gamma_Z t$. The dashed lines show $\gamma_Z = |\alpha|^2\kappa_Z$.

formula fits the numerical simulations perfectly and exponentially small gate errors are achieved. As κ_Z is increased, we find a deviation from the optimal gate errors due to the competition with two-photon dissipation, as the cat significantly leaves the code space of intended size $|\alpha|^2$ during the gate, getting drawn closer to the vacuum. An exponential scaling with time is maintained, although with a smaller exponential rate, as discussed in Sec. VIII B.

In Fig. 10(c), we extract this exponential scaling rate from a linear fit of $\gamma(t) = -\ln(p_Z(t))$, which yields γ_Z such that $p_Z(t) \sim \exp(-\gamma_Z t)$ for sufficiently large time values. This exponential rate is then plotted as a function of κ_Z/κ_2 for varying values of $|\alpha|^2$ and also compared to the ideal rate of Eq. (36), given by $\gamma_Z = |\alpha|^2\kappa_Z$. Again, a transition from the optimal gate-error regime to a suboptimal regime is found as κ_Z/κ_2 is increased. In addition, the point of transition scales as α, which would confirm the limit of validity of the optimal regime given by $\alpha\kappa_Z \ll 4|\alpha|^2\kappa_2$ or, equivalently, $\kappa_Z/\kappa_2 \ll 4\alpha$.

The effect of κ_Z/κ_2 on *bit-flip* errors is investigated in Fig. 10(b). In this particular simulation, a relatively large gate time is fixed at $T = 10/\kappa_2$ to ensure the relevance of the study. We find that bit errors are indeed suppressed exponentially according to $p_X \propto \exp(-2|\alpha|^2)$ for all values of κ_Z investigated, thus preserving the error bias of cat qubits. However, as the effective cat size is reduced by the κ_Z term of Eq. (35a) during the gate time, the prefactor of this exponential increases linearly with κ_Z/κ_2.

The main side process limiting the fidelity of discrete gates would be the ancillary-mode lifetime. Since the gate is based on a transition from the ground to the excited state of the ancilla that will serve as a photon blocker, any unwanted transition between these two ancillary states will perturb the gate process. In Fig. 11, we investigate finite qubit lifetimes for the two-level ancillary mode. Here, a discrete $Z(\pi)$ gate is simulated numerically in the presence of single-photon losses on the ancillary qubit of the form $\kappa_q\mathcal{D}[\sigma_-]$, with varying values of κ_q/κ_2. An analytical fit is further shown for each numerical simulation, which reads $p_Z(t) = \kappa_q t + \exp(-|\alpha|^2\kappa_Z t)$ and matches each line very well. Indeed, ancillary-mode losses induce unwanted $|e\rangle \to |g\rangle$ transitions at a constant rate, which are followed exponentially quickly by a $|g\rangle \to |e\rangle$ transition of the discrete gate correlated dissipator, inducing a second phase flip and hence canceling the $Z(\pi)$ gate. Thermal excitations of the ancillary mode would have a similar effect by activating the $|g\rangle \to |e\rangle$ transition without a cat-mode parity switch but in a cold environment, such excitations have a much smaller rate than qubit decay.

While this linear increase of phase errors may appear limiting for the usefulness of the gate design, we recall that finite lifetime of the cat oscillator also induces phase errors that scale linearly in time, according to $p_Z = |\alpha|^2\kappa_1 t$, where κ_1 is the rate of single-photon losses. Those losses are inevitable without changing the overall cat-qubit encoding. In contrast, for the ancilla, while a transmonlike qubit would yield a simple gate implementation, the particular gate design is compatible with more specific quantum systems. There is no requirement for the protection of the $|g\rangle + |e\rangle \leftrightarrow |g\rangle - |e\rangle$ transition, since only the diagonal elements are used by the gate design. As such, any ancilla system that can robustly implement a single transition from $|g\rangle$ to $|e\rangle$ would suffice for better gate protection. One can think of a three-level Λ system with two metastable ground states [63,64] or a system where the ancilla state would escape (but never return to $|g\rangle$) after reaching $|e\rangle$.

In Fig. 12, we investigate other gate angles, $\theta \neq \pi$, both with the ancillary two-level system design of Eq. (33) [Fig. 12(a)] and with the three-level system design of Eq. (38) that cancels out parity switching in the $|g\rangle\langle g|$ subspace through interference [Fig. 12(b)]. In the first scheme, the phase errors first scale exponentially until they hit a plateau corresponding to the parity-switching leakage of Eq. (37). This plateau scales according to $\sin^2(\theta)$. With

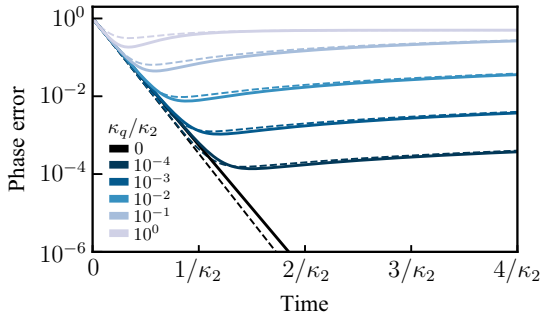

FIG. 11. The gate-induced phase errors of a discrete $Z(\pi)$ gate as in Eq. (33) with additional single-photon losses of the form $\kappa_q\mathcal{D}[\sigma_-]$ on the ancillary qubit. The dashed lines show $p_Z = \kappa_q t + \exp(-|\alpha|^2\kappa_Z t)$. The cat size is fixed at $|\alpha|^2 = 8$ and $\kappa_Z/\kappa_2 = 1$.

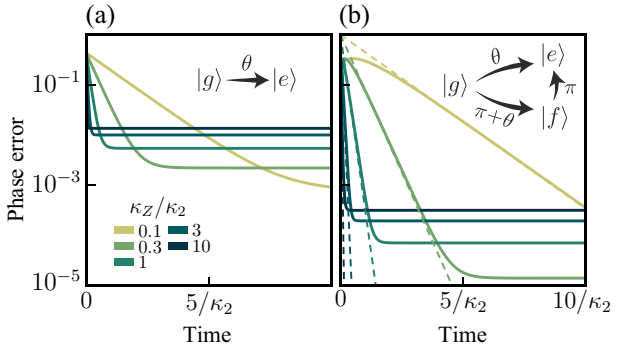

FIG. 12. The gate-induced phase errors of a discrete $Z(\pi/3)$ gate, with the designs of (a) Eq. (33), using an ancillary two-level system, and (b) Eq. (38), using an ancillary three-level system. The dashed lines show $p_Z = \exp(-|\alpha|^2\kappa_Z t)$. The insets show the gate transitions between ancillary states for either design.

the qutrit scheme, the exponential scaling of phase errors is also observed but for longer time scales, thus confirming that the parity-switching dynamics are canceled out. A plateau is still hit after some time t but at lower phase errors than for the previous two-level system scheme. This new limitation is explained by the fact that if the state is initially not coherent or with a different coherent-state amplitude than α, $\mathbf{a}_\theta$ does not map exactly onto a $Z(\theta)$ gate. Since the $|g\rangle\langle g|$ subspace dynamics induce such incoherent fluctuations, the gate fidelities are limited by this effect. For sufficiently small values of κ_Z/κ_2, however, the state stays inside the code space at all times and the exponential scaling of gate errors is maintained for longer time scales.

D. Multiqubit gates

Regarding multiqubit gates, the single-qubit discrete method of Eq. (33) can be generalized but not necessarily in a trivial manner. For CZ gates, consider the two-qubit operator

$$\mathbf{L}_{\mathrm{CZ}} = -\mathbf{a}_1(\mathbf{a}_2 - \alpha) + \alpha(\mathbf{a}_2 + \alpha), \tag{40}$$

where $\mathbf{a}_{1/2}$ are the annihilation operators on each mode involved. This operator is such that $\mathbf{L}_{\mathrm{CZ}}|\pm\alpha\rangle_1|\alpha\rangle_2 = 4\alpha|\pm\alpha\rangle_1|\alpha\rangle_2$ and $\mathbf{L}_{\mathrm{CZ}}|\pm\alpha\rangle_1|-\alpha\rangle_2 = \pm 4\alpha|\pm\alpha\rangle_1|\alpha\rangle_2$, which thus meets the CZ-gate requirements. Note in particular the interchangeability of $\mathbf{a}_1$ and $\mathbf{a}_2$ in this operator, which shows the CZ-gate symmetry. By engineering a dissipation of the form $\mathcal{D}[\mathbf{L}_{\mathrm{CZ}}\boldsymbol{\sigma}_+]$, an exponentially scaling CZ gate can be achieved. It would, however, suffer from the same issues as qubit-enabled $Z(\theta)$ gates due to the $|g\rangle\langle g|$ parity-switching dynamics, since $\mathbf{L}^\dagger_{\mathrm{CZ}}\mathbf{L}_{\mathrm{CZ}}$ contains parity-switching terms in both $\mathbf{a}_1$ or $\mathbf{a}_2$. Similarly as for single-qubit $Z(\theta)$ rotations, it is possible to cancel out these terms through interference by instead using four operators similar to $\mathbf{L}_{\mathrm{CZ}}$ and a higher-dimensional ancillary system.

For CNOT gates, consider the two-qubit operator

$$\mathbf{L}_{\mathrm{CX}} = \alpha\mathbf{I}\otimes\mathbf{P}_+ + \mathbf{a}\otimes\mathbf{P}_-, \tag{41}$$

where the first and second modes in this outer product are control and target qubits, respectively, where $\mathbf{I}$ is the oscillator identity, and where $\mathbf{P}_\pm = (e^{i\pi\mathbf{a}^\dagger\mathbf{a}} \pm 1)/2$ are projectors on the even- and odd-parity subspaces of the target mode, respectively. Similarly as for the single-mode method, engineering a correlated dissipator with an ancillary-qubit mode of the form $\mathcal{D}[\mathbf{L}_{\mathrm{CX}}\boldsymbol{\sigma}_+]$ would achieve a discrete CNOT gate, up to exponentially small corrections. However, the projection operators $P_\pm$ are highly nonlocal and therefore this scheme is of questionable use. First, such operators are not currently implementable with superconducting circuits, although there is a path toward them as high-impedance operators [65]. Second, if one assumes access to such "next-generation" operators, then for fairness one should view as also relatively easy the options of, e.g., Sec. VII. Third, engineering nonlocal operators in a cat-qubit context is a Pandora's box, as it introduces artificial operators against which the exponential bit-flip protection is *not* designed to work.

Other designs may take inspiration from the Zeno implementation of the CNOT gate, i.e., inducing, in superposition, $n - n_p$ discrete $Z(\theta)$ gates on the control qubit conditional on Fock state n in the target qubit. In the Zeno Hamiltonian implementation, this indeed remains compatible with exponential bit-flip protection. Generalizing this to a jump operator appears to require a complicated ancilla system. For instance, if we were to rely on $n - n_p$ ancilla jumps to perform the right number of $Z(\theta)$ gates, then Fock-number information would leak out to the environment unless specific erasure actions were taken to impede detection of the number of jumps. In the absence of concrete insights into realistic experimental building blocks associated with such an ancilla, we leave this for future research.

Barring the experimental difficulty of realizing an operator such as $\mathbf{L}_{\mathrm{CX}}$, the effect of unwanted $|g\rangle \leftrightarrow |e\rangle$ transitions of the ancillary mode that monitors the gate warrants a caveat. Indeed, an unwanted transition would mean possibly applying the CNOT gate an even number of times, which would by definition involve both phase-flip and bit-flip errors. In the traditional model, bit-flip errors remain exponentially suppressed even for CNOT gates, due to a smart use of the available continuous phase space, which we lose with this design. On the upside, the particular use of the ancillary qubit in this discrete gate opens the door to specific designs reducing ancilla-induced errors, as discussed above for the $Z(\theta)$ gate.

IX. CONCLUSIONS

We have introduced four new designs of dissipative cat-qubit gates that can help reduce gate-induced phase errors and therefore help reach error-correction thresholds. Upon the observation that incoherent gate errors result from the entanglement between the cat qubit and its buffer mode, we have devised two designs meant to take advantage of the buffer memory in the system. The first one is based on the photodetection of the buffer-mode output and thus on the retrieval of information that can then be classically fed back. The precision of this scheme is only limited by the photodetector efficiency. The second one relies on an autonomous error-correcting scheme for which first-order gate-induced parity errors are automatically corrected for as buffer photons exit the resonator. In particular, this second design is readily implementable with superconducting circuits and achieves a reduction of up to 2 orders of magnitude in gate errors. The same setup can also be used with squeezed cat states for the autonomous correction

of single-photon losses [51], currently one of the main limiting factors of bosonic qubits.

We have also described two drastically different gate designs. By engineering higher-order drive Hamiltonians that feature locally flat energy potentials in position representation, spurious effects on the cat-qubit mode can be avoided and an improvement in gate-error fidelities is achieved. We believe that such Hamiltonians could also be used for other purposes, such as cat-state preparation. Finally, we have explored how to engineer cat-qubit gates without the Zeno effect and introduced dissipation-based gate engineering. By coupling the cat mode to an ancillary nonlinear mode that monitors the ongoing gate, a discrete π-phase gate is realized. This method can circumvent the usual linear gate-time scaling of Zeno-based gates and achieve exponentially scaling gate fidelities and associated CNOT-gate designs are therefore the subject of our ongoing investigations.

We hope that this paper has been able to provide its readers with intuition about the design of cat-qubit gates. While we have explored many paths toward high-fidelity gates, we believe that further improvements can still be achieved, in particular for multimode encodings of cat qubits. Finally, while these gate designs have been particularly focused on dissipative cat qubits, they should also inspire the design of superadiabatic operations on any bosonic or dissipatively stabilized system. In particular, most tailored-dissipation operators often rely on a highly damped buffer mode together with adiabatic elimination. We have thus described for the first time how one can take advantage of the dynamics of this buffer mode.

ACKNOWLEDGMENTS

We thank Benjamin Huard, Pierre Rouchon, Lev-Arcady Sellem, and Jérémie Guillaud for fruitful discussions. This work was supported by the French Agence nationale de la recherche under Grant No. ANR-18-CE47-0005. We also acknowledge funding from Plan France 2030 through the project ANR-22-PETQ-0006. The numerical simulations were performed using high-performance computing resources at Inria Paris and using the QuTIP open-source package. We thank the QuTIP developers and maintainers for their work.

APPENDIX A: REVIEW OF THE SHIFTED FOCK BASIS

In this appendix, we review the shifted Fock basis (SFB) as first introduced in Ref. [37]. We refer to the original paper for a full review of the method, but this short appendix provides the minimal elements required for the comprehension of the main text.

The SFB is an alternative basis of states for a quantum oscillator that splits the main properties of a cat qubit into two separate modes: a qubit mode that represents the logical cat-qubit state and a gauge mode that represents leakage away from the stabilized computational subspace of Eq. (3). More precisely, let us define the nonorthonormal basis states

$$|\pm, n\rangle \equiv \frac{1}{\sqrt{2}}\left[\mathbf{D}(\alpha) \pm (-1)^n \mathbf{D}(-\alpha)\right] |\mathbf{n} = n\rangle \tag{A1}$$

where $\mathbf{D}(\alpha)$ is the displacement operator and $|\mathbf{n} = n\rangle$ is the nth Fock state. These states are such that, in the ground-state manifold $n = 0$, they match the cat-qubit computational basis states, i.e., $|\pm, 0\rangle \propto |\pm\rangle_L$. Although these states do not define an orthonormal basis, any two states in a separate $\pm$ branch are exactly orthogonal due to the even or odd parity in the number of photons. In addition, the first shifted Fock states are approximately orthonormal in the limit of $|\alpha| \gg 1$. To treat this basis rigorously, it can be orthornormalized with, e.g., a Gram-Schmidt process, but we again refer to Ref. [37] for details.

A particularly interesting property of the SFB is how it transforms the annihilation operator $\mathbf{a}$. Indeed, acting on the basis states of Eq. (A1) yields

$$\begin{aligned} \mathbf{a}\,|\pm, n\rangle &= \sqrt{n}\,|\mp, n-1\rangle + \alpha\,|\mp, n\rangle \\ &= \boldsymbol{\sigma}_z \otimes (\tilde{\mathbf{a}} + \alpha)\,|\pm, n\rangle\,, \end{aligned} \tag{A2}$$

where we have defined two new operators $\boldsymbol{\sigma}_z$ and $\tilde{\mathbf{a}}$ such that $\boldsymbol{\sigma}_z\,|\pm, n\rangle = |\mp, n\rangle$ and $\tilde{\mathbf{a}}\,|\pm, n\rangle = \sqrt{n}\,|\pm, n-1\rangle$, in analogy to a qubit and a quantum oscillator mode. From Eq. (A2), we infer the mapping of the annihilation operator from the Fock to the shifted Fock basis, which reads

$$\mathbf{a} \to \boldsymbol{\sigma}_z \otimes (\tilde{\mathbf{a}} + \alpha). \tag{A3}$$

Again, this mapping is only valid in the limit of small shifted Fock excitation numbers because of the nonorthonormalization of the basis. It is, however, very helpful for understanding the intimate dynamics of cat-qubit gates and for the numerical analysis of phase-flip errors.

In particular, it is possible to derive the probability of phase errors induced by cat-qubit gates up to first order in the dynamics. This derivation has been done extensively in Ref. [37], so we only give these results again here for completeness. For single-qubit $Z(\theta)$ gates, the probability of nonadiabatic phase errors reads

$$p_Z = \frac{\theta^2}{16|\alpha|^4 \kappa_2 T}, \tag{A4}$$

where $\kappa_2 \equiv 4g_2^2/\kappa_b$ in the presence of two-photon exchange coupling with a buffer mode. For two-qubit CNOT gates, nonadiabatic phase errors only affect control qubits

and read

$$p_{Z_C} = \frac{\pi^2}{16|\alpha|^2\kappa_2 T}, \quad p_{Z_T} = p_{Z_T Z_C} = 0, \tag{A5}$$

where the subscripts C and T stand for control and target qubits, respectively.

APPENDIX B: EFFECT OF NOISE AND SPURIOUS HAMILTONIANS

In the main text, we study gate designs with simplified master-equation models in order to capture the key elements of each proposal. However, actual experimental setups feature various sources of errors that could, in principle, hinder gate performance. In this appendix, we study a more complete model of errors to demonstrate that our proposals hold even under realistic noise processes.

The master equation that we consider is

$$\frac{d\boldsymbol{\rho}}{dt} = \mathcal{L}_0\boldsymbol{\rho} - i\,[\mathbf{H}_s, \boldsymbol{\rho}] + \kappa_a(1+n_{\mathrm{th},a})\mathcal{D}[\mathbf{a}]\boldsymbol{\rho} + \kappa_a n_{\mathrm{th},a}\mathcal{D}[\mathbf{a}^\dagger]\boldsymbol{\rho} + \kappa_{\phi,a}\mathcal{D}[\mathbf{a}^\dagger\mathbf{a}]\boldsymbol{\rho}, \tag{B1}$$

where $\mathcal{L}_0$ denotes the Liouvillian to be engineered on the system—varied from one gate design to the next—which typically contains two-to-one photon exchange, buffer-mode dissipation, and a gate drive on the memory mode, and

$$\mathbf{H}_s = -K_a\mathbf{a}^{\dagger 2}\mathbf{a}^2 + \chi_{ab}\mathbf{a}^\dagger\mathbf{a}\mathbf{b}^\dagger\mathbf{b} - K_b\mathbf{b}^{\dagger 2}\mathbf{b}^2 \tag{B2}$$

is a spurious Hamiltonian with Kerr and cross-Kerr terms on the memory and buffer modes. These terms typically result from the residual cosine potential in the full-circuit Hamiltonian but, in practice, they can be small compared to two-photon dissipation when the system is engineered with an ATS at the appropriate flux bias point [42]. Our master-equation model also includes single-photon losses, thermal photons, and pure dephasing on the memory mode with respective rates κ_a, $n_{\mathrm{th},a}$ and $\kappa_{\phi,a}$. Note that we do not include thermal photons on the buffer mode in this model, as they are discussed separately in Appendix C.

To study these noise processes, we consider specific values for each term mainly extracted from Refs. [42,66]. The two-to-one photon exchange coupling is $g_2/2\pi = 1$ MHz and is combined with a buffer-mode dissipation at $\kappa_b/2\pi = 8$ MHz that yields an effective two-photon dissipation rate $\kappa_2/2\pi = 500$ kHz. The Kerr and cross-Kerr energies are $K_a/2\pi = 1$ kHz, $K_b/2\pi = 810$ kHz, and $\chi_{ab}/2\pi = 65$ kHz. The single-photon loss is $\kappa_a/2\pi = 53$ Hz, corresponding to $T_1 = 3$ ms in the memory mode, which is typical in current experiments with high-Q superconducting resonators. Note that lower cavity lifetimes could also be investigated but would limit the potential gain in gate fidelity of our proposals compared to standard Zeno gates, as phase errors would be dominated by single-photon losses in this regime. Finally, thermal noise and pure dephasing are $n_{\mathrm{th},a} = 10\%$ and $\kappa_{\phi,a}/2\pi = 10$ Hz.

In Fig. 13, gate errors under this noise model are shown for each gate design from the main text. In each case, the performance is compared to the standard Zeno gate for a $Z(\pi)$ gate, shown as black lines. In all panels, the phase errors eventually converge to a linear dependence in the large-gate-time regime, in which single-photon losses are dominant. In addition, there is, systematically, an optimal gate time that minimizes gate errors and that represents the optimal trade-off between gate-induced and single-photon loss errors.

For the photodetection design in Fig. 13(a), we vary the photodetection efficiency from a perfect photodetector ($\eta = 1$) to a nonideal one at $\eta = 0.5$, demonstrating again the linear dependence with detection inefficiency as discussed in the main text. In Fig, 13(b), we show the performance of the autonomous-feedback design with $\kappa_{ab}/2\pi = 2$ MHz and $\kappa_b = 0$. In Fig. 13(c), we show the

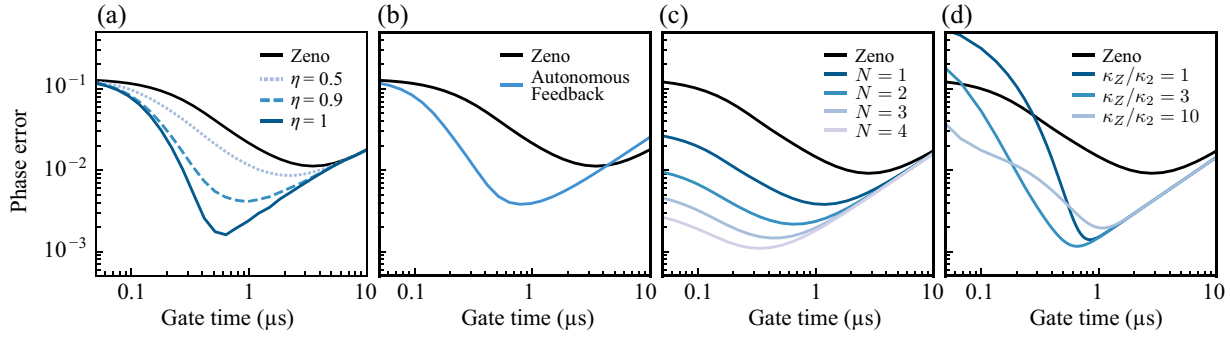

FIG. 13. The phase errors during a $Z(\pi)$ gate under a complete model of noise for each gate design introduced in the main text: (a) photodetection; (b) autonomous feedback; (c) locally flat Hamiltonian; (d) discrete jump. Each design is compared to the standard Zeno gate (black). In all panels, $|\alpha|^2 = 4$ and energies are set to $g_2/2\pi = 1$ MHz, $K_a/2\pi = 1$ kHz, $K_b/2\pi = 810$ kHz, $\chi_{ab}/2\pi = 65$ kHz, $\kappa_a/2\pi = 53$ Hz, $n_{\mathrm{th},a} = 10\%$, and $\kappa_{\phi,a}/2\pi = 10$ Hz. For (a), (c), and (d), $\kappa_b/2\pi = 8$ MHz. For (b), $\kappa_{ab}/2\pi = 2$ MHz.

locally flat Hamiltonian design for an increasing number of odd drive terms from $N = 1$ to $N = 4$, each time gaining in optimal gate fidelity and gate time. Finally, in Fig. 13(d), we show the performance of the discrete jump design, where the optimal gate fidelity depends on the ratio of κ_Z to κ_2 and on the actual error model studied.

APPENDIX C: THERMAL NOISE IN THE BUFFER MODE

In this appendix, we discuss the role of thermal noise in the buffer mode for the first two designs based on the feedback of information introduced in the main text. Since these two schemes use the buffer-mode population to detect potential phase flips induced on the memory mode, it is quite natural that one of their main limitations should come from spurious population in the buffer.

1. Photodetection

For the photodetection scheme of Sec. V, the feedback action to apply is a $Z(\pi)$ gate after every buffer-photon detection. Therefore, the rate of thermal photons is directly linked to the rate of phase information loss on the cat state, assuming that the feedback action is perfect. From the point of view of the SFB, one can adiabatically eliminate the gauge mode in Eq. (21) and average out the stochastic terms. This leads to a simplified model in the absence of a gate drive,

$$\begin{aligned}\frac{d\boldsymbol{\rho}}{dt} &= \kappa_b\eta(1+n_{\mathrm{th},b})\mathcal{D}[\mathbf{b}\boldsymbol{\sigma}_z]\boldsymbol{\rho}\\ &+ \kappa_b(1-\eta)(1+n_{\mathrm{th},b})\mathcal{D}[\mathbf{b}]\boldsymbol{\rho}\\ &+ \kappa_b n_{\mathrm{th},b}\mathcal{D}[\mathbf{b}^\dagger]\boldsymbol{\rho}. \end{aligned} \tag{C1}$$

Here, the beam-splitter interaction between the gauge and buffer modes is eliminated compared to the fast dynamics on the buffer. In particular, note the correlated dissipation in $\mathcal{D}[\mathbf{b}\boldsymbol{\sigma}_z]$, which arises from the idealized classical feedback action on the memory mode. From this master equation, we easily compute the average expectation value of the $\boldsymbol{\sigma}_x$ operator by going to the Heisenberg picture, which reads

$$\langle\boldsymbol{\sigma}_x\rangle(t) = \langle\boldsymbol{\sigma}_x\rangle(t=0)\times\exp(-\gamma t), \tag{C2}$$

where $\gamma = 2\eta\kappa_b n_{\mathrm{th},b}(1+n_{\mathrm{th},b})$ is the rate of parity-information loss in the presence of thermal noise in the buffer. Note that the classical feedback action is always optional and typically it should only be turned on during gates. To know whether the gate design is beneficial in practice, this rate should be compared to the rate of single-photon losses κ_a, which is the usual dominant source of loss of parity information.

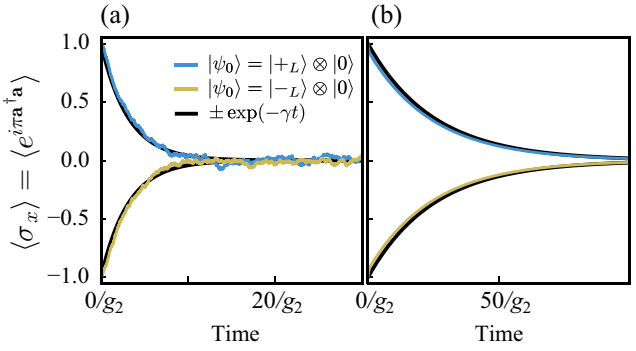

FIG. 14. (a) The photon-number parity of an idling cat state under the photodetection and classical feedback design of Sec. V, with thermal noise in the buffer mode $n_{\mathrm{th},b} = 2\%$. Parity is averaged over 1000 stochastic trajectories and fitted with an exponential decay at rate $\gamma = 2\eta\kappa_b n_{\mathrm{th},b}(1+n_{\mathrm{th},b})$. In this simulation, $\kappa_b/g_2 = 8$, $|\alpha|^2 = 8$ and $\eta = 1$. (b) The photon-number parity of an idling cat state under the autonomous feedback of Sec. VI, with thermal noise in the reservoir mode $n_{\mathrm{th},r} = 2\%$. Parity is fitted with an exponential decay at rate $\gamma = 2\sqrt{g_2\kappa_{ab}}n_{\mathrm{th},r}$. In this simulation, $\kappa_{ab}|\alpha|^2/g_2 = 8$ and $|\alpha|^2 = 8$.

In Fig. 14(a), we show the parity of an idling cat state initialized in $|\pm_L\rangle$ as obtained from numerical integration of the full stochastic master equation (i.e., including two-photon coupling, buffer-mode dissipation, and thermal noise in the buffer). The solution is averaged over 1000 stochastic trajectories and we find a very good fit with the simplified model as described above.

2. Autonomous feedback

For the feedback design of Sec. VI, the feedback action is this time performed autonomously through a correlated dissipation operator in $\mathcal{D}[\mathbf{ab}]$. Buffer excitations would then also result in spurious parity swaps on the cat mode. However, with this design, the buffer mode is *a priori* a high-Q mode, since the correlated dissipation is engineered through a third reservoir mode $\mathbf{r}$, as discussed in the main text, with a three-mode coupling of the form $g(\mathbf{abr}^\dagger + \text{h.c.})$. Therefore, the main limitation of this design does not come from buffer-mode excitations but, rather, from thermal noise in the reservoir mode in the form $\kappa_r n_{\mathrm{th},r}\mathcal{D}[\mathbf{r}^\dagger]$. From adiabatic elimination of this reservoir with the formalism of Refs. [52,53], we derive an effective rate of correlated excitations. The effective master equation on the memory and buffer modes for an idling cat qubit thus reads

$$\begin{aligned}\frac{d\boldsymbol{\rho}}{dt} &= -i[\mathbf{H}_{AB},\boldsymbol{\rho}]\\ &+ \kappa_{ab}(1+n_{\mathrm{th},r})\mathcal{D}[\mathbf{ab}]\boldsymbol{\rho}\\ &+ \kappa_{ab}n_{\mathrm{th},r}\mathcal{D}[\mathbf{a}^\dagger\mathbf{b}^\dagger],\boldsymbol{\rho} \end{aligned} \tag{C3}$$

where a new term in $\mathcal{D}[\mathbf{a}^\dagger\mathbf{b}^\dagger]$ appears compared to the ideal master equation. This dissipation creates correlated excitations on the memory and buffer modes. If these correlated excitations are dissipated through the $\mathcal{D}[\mathbf{ab}]$ term, then the parity is swapped back to its original value and no phase information is lost. However, the correlated excitation can also undergo partial two-photon Rabi oscillations through the $\mathbf{H}_{AB}$ term and then eventually dissipate away. In this case, the parity is not strictly preserved by the dynamics and phase information is lost to the environment.

In Fig. 14(b), we show the parity of an idling cat state initialized in $|\pm_L\rangle$ as obtained from the numerical integration of Eq. (C3). We indeed find that the parity information decays exponentially with a rate γ. For all the values of g_2, κ_{ab}, and $n_{\mathrm{th},r}$ that we have investigated, this rate seems to fit the formula $\gamma = 2\sqrt{g_2\kappa_{ab}}n_{\mathrm{th},r}$. In particular, turning off either two-to-one photon coupling or thermal noise on the reservoir mode suppresses this effect.

APPENDIX D: MASTER-EQUATION INVARIANCE BY JOINT PHASE CONJUGATION

In this appendix, we show how the Lindblad master equation of a $Z(\theta)$ gate is invariant under a joint x-axis phase conjugation of the cat and buffer modes.

1. Phase-conjugation superoperator

An x-axis phase conjugation consists in flipping the sign of quadrature $\mathbf{x}$ while keeping quadrature $\mathbf{p}$ unchanged [67]. While this is an unphysical transformation—it does not preserve commutation relations—it can be understood as a time-reversal operator. It is also a standard example of a superoperator that is positive but not completely positive [68]. In our case, the symmetry of the master equation by joint phase conjugation implies that the logical bit information of the cat qubit (encoded in the x axis) is also encoded in the x axis of the buffer mode and so in an exact manner.

Let us first define the x-axis phase-conjugation superoperator on a single mode, which we denote as $\mathcal{C}$. By definition, this superoperator is such that $\mathcal{C}\,|x\rangle\langle x| = |-x\rangle\langle -x|$ and $\mathcal{C}\,|p\rangle\langle p| = |p\rangle\langle p|$, where $|x\rangle$ and $|p\rangle$ are quadrature eigenstates. By linearity, the identities $\mathcal{C}\mathbf{x} = -\mathbf{x}$ and $\mathcal{C}\mathbf{p} = \mathbf{p}$ follow directly, since $\mathbf{x} = \int dx\, x\rangle\langle x|$ and $\mathbf{p} = \int dp\, |p\rangle\langle p|$. More generally, we have that $\mathcal{C}f(\mathbf{x}) = f(-\mathbf{x})$ for any function f. Reinserting $|x\rangle = \int dp\, \mathrm{e}^{-ipx}|p\rangle$ in this identity, we have that

$$\int dx f(x) \iint dpdp' \mathrm{e}^{-i(p-p')x}\mathcal{C}\,|p\rangle\langle p'| = \int dx f(x) \iint dpdp' \mathrm{e}^{i(p-p')x}\,|p\rangle\langle p'|. \tag{D1}$$

Rearranging the integrals and denoting by $\tilde{f}(p)$ the Fourier transform of $f(x)$, Eq. (D1) reads

$$\iint dpdp' \tilde{f}(p-p')\left(\mathcal{C}\,|p\rangle\langle p'| - |p'\rangle\langle p|\right) = 0. \tag{D2}$$

Since this equation holds for any function $\tilde{f}$, then we have that $\mathcal{C}\,|p\rangle\langle p'| = |p'\rangle\langle p|$, and similarly for the other quadrature, $\mathcal{C}\,|x\rangle\langle x'| = |-x'\rangle\langle -x|$. In particular, note the transposition in both of these relations, which accounts for the time-reversal property of the conjugation.

Before moving on, there is a last identity that will be useful for our upcoming derivation. For any density matrix $\boldsymbol{\rho}$, we have

$$\begin{aligned}\mathcal{C}(\mathbf{x}\boldsymbol{\rho}) &= \mathcal{C}\left(\iint dxdx' x\rho(x,x')\,|x\rangle\langle x'|\right)\\ &= \iint dxdx' x\rho(x,x')\,|-x'\rangle\langle -x|\\ &= \iint dx'dx(-x')\rho(-x',-x)\,|x\rangle\langle x'|\\ &= -\mathcal{C}(\boldsymbol{\rho})\mathbf{x}.\end{aligned} \tag{D3}$$

Using that $\mathcal{C}^2$ yields the identity superoperator, we directly obtain the converse identity, $\mathcal{C}(\boldsymbol{\rho}\mathbf{x}) = -\mathbf{x}\mathcal{C}(\boldsymbol{\rho})$. Similarly for the other quadrature, we have that $\mathcal{C}(\mathbf{p}\boldsymbol{\rho}) = \mathcal{C}(\boldsymbol{\rho})\mathbf{p}$ and $\mathcal{C}(\boldsymbol{\rho}\mathbf{p}) = \mathbf{p}\mathcal{C}(\boldsymbol{\rho})$.

2. Master-equation invariance

Our goal is now to show that the joint phase conjugation of the cat and buffer modes is a symmetry of the $Z(\theta)$ gate dynamics. This involves showing that the joint phase-conjugation superoperator $\mathcal{C}_{AB} = \mathcal{C}_A \otimes \mathcal{C}_B$ commutes with the Lindblad superoperator $\mathcal{L}$, where

$$\mathcal{L} = \mathcal{L}_Z + \mathcal{L}_{AB} + \mathcal{L}_{1,A} + \mathcal{L}_{1,B}, \tag{D4}$$

in which $\mathcal{L}_Z = -i[\mathbf{H}_Z, \cdot\,]$, $\mathcal{L}_{AB} = -i[\mathbf{H}_{AB}, \cdot\,]$, $\mathcal{L}_{1,A} = \kappa_a\mathcal{D}[\mathbf{a}]$, and $\mathcal{L}_{1,B} = \kappa_b\mathcal{D}[\mathbf{b}]$. By linearity, it is sufficient to show the commutation relation for each term in the Lindblad superoperator. For the single-mode cavity drive with Hamiltonian $\mathbf{H}_Z = \varepsilon_Z\mathbf{x}_a$, we obtain

$$\begin{aligned}\mathcal{C}(\mathcal{L}_Z(\boldsymbol{\rho})) &= -i\varepsilon_Z\mathcal{C}(\mathbf{x}_a\boldsymbol{\rho} - \boldsymbol{\rho}\mathbf{x}_a)\\ &= -i\varepsilon_Z\left(-\mathcal{C}(\boldsymbol{\rho})\mathbf{x}_a + \mathbf{x}_a\mathcal{C}(\boldsymbol{\rho})\right)\\ &= \mathcal{L}_Z(\mathcal{C}(\boldsymbol{\rho})).\end{aligned} \tag{D5}$$

For the two-photon exchange term, the Hamiltonian reads $\mathbf{H}_{AB} = g_2(\mathbf{a}^2 - \alpha^2)\mathbf{b}^\dagger + \mathrm{h.c.}$. Rewriting the Hamiltonian

in terms of quadrature operators yields

$$\mathbf{H}_{AB}/g_2 = (\mathbf{x}_a^2 - \mathbf{p}_a^2)\frac{\mathbf{x}_b}{4} + (\mathbf{p}_a\mathbf{x}_a + \mathbf{x}_a\mathbf{p}_a)\frac{\mathbf{p}_b}{4} - \alpha^2\mathbf{x}_b. \tag{D6}$$

Since this Hamiltonian features only terms with an odd number of quadrature $\mathbf{x}$ and even number of quadrature $\mathbf{p}$ operators, use of the identities in Eq. (D3) and the related ones yields an overall minus sign and a transposition, from which we infer that

$$\mathcal{C}(\mathcal{L}_{AB}(\boldsymbol{\rho})) = \mathcal{L}_{AB}(\mathcal{C}(\boldsymbol{\rho})). \tag{D7}$$

Finally, for the single-photon loss operators on either mode $\mathcal{L}_1 = \mathcal{D}[\mathbf{x} + i\mathbf{p}]$, and again using the Eq. (D3) identities,

$$\begin{aligned}\mathcal{C}\big(\mathcal{L}_1(\boldsymbol{\rho})\big) &= \mathcal{C}\big((\mathbf{x}+i\mathbf{p})\cdot\boldsymbol{\rho}\cdot(\mathbf{x}-i\mathbf{p})\big) \\ &\quad - \mathcal{C}\big((\mathbf{x}^2+\mathbf{p}^2)\cdot\boldsymbol{\rho}\big)/2 \\ &\quad - \mathcal{C}\big(\boldsymbol{\rho}\cdot(\mathbf{x}^2+\mathbf{p}^2)\big)/2 \\ &= (\mathbf{x}+i\mathbf{p})\cdot\mathcal{C}(\boldsymbol{\rho})\cdot(\mathbf{x}-i\mathbf{p}) \\ &\quad - \mathcal{C}(\boldsymbol{\rho})\cdot(\mathbf{x}^2+\mathbf{p}^2)/2 \\ &\quad - (\mathbf{x}^2+\mathbf{p}^2)\cdot\mathcal{C}(\boldsymbol{\rho})/2 \\ &= \mathcal{L}_1(\mathcal{C}(\boldsymbol{\rho})).\end{aligned} \tag{D8}$$

By linearity, the required result is shown: $\mathcal{C}\mathcal{L} - \mathcal{L}\mathcal{C} = 0$. This shows the invariance of the $Z(\theta)$ gate master equation under a joint x-axis phase conjugation of both cat and buffer modes.

APPENDIX E: IDEAL FEEDBACK FOR PHOTODETECTION

In this appendix, we discuss the ideal feedback action to be applied for the photodetection design of V. Assuming a perfect photodetector with detection efficiency $\eta = 1$ and instantaneous feedback, this ideal feedback can yield errorless gates. Indeed, if $\eta = 1$, then no information is lost to the environment and the combined qubit-buffer state remains pure at all times, such that the final cat-qubit state is pure. An appropriate feedback action can thus retrieve the desired angle of rotation.

In Fig. 15, we show the profiles of the optimal feedback angles $\pi + \delta(t_J)$ upon photon detection, as a function of detection time t_J, for a targeted $Z(\pi)$ gate. The mean photon population of the buffer mode is also shown as a function of time and is proportional to the instantaneous photodetection probability $\langle dN_\eta\rangle$. Note that close to $t = T$ in the middle plot, the angle δ diverges to negative values but $\langle\mathbf{b}^\dagger\mathbf{b}\rangle \ll 1$ at this time, such that it is excessively unlikely to ever have to perform this feedback action.

To perform this classical feedback upon detection of buffer photons, multiple solutions exist. The first and most straightforward is to actually add this $Z(\pi + \delta)$ gate to the actuation, which would *occasionally* increase the gate time, depending on the input-gate angle θ and the detection time t_J. For instance, if a photon is detected at the beginning of a $Z(0.9\pi)$ gate, then a shorter $Z(-0.1\pi + \delta)$ gate should be performed instead, while if it is detected toward the end, then a longer $Z(1.9\pi + \delta)$ gate would be realized. While this happens only for photon-detected trajectories and thus with low probability, it causes unpredictable gate times.

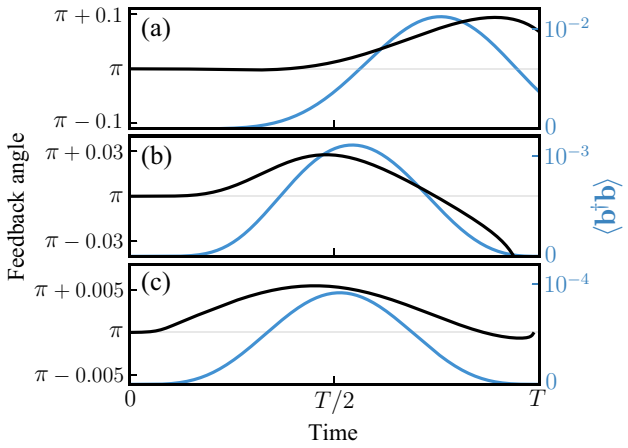

FIG. 15. The angle of the Z rotation feedback (in black) to perform after a buffer-mode photodetection at any given time, for a $Z(\pi)$ gate of duration T, and the buffer-mode population for the no-jump trajectory (in blue), proportional to the photodetection probability $\langle dN_\eta\rangle$: (a) $T = 1/g_2$; (b) $T = 3/g_2$; (c) $T = 10/g_2$. In these numerical simulations, $\kappa_b = 8g_2$ and $|\alpha|^2 = 8$.

As a second option, the feedback could adjust the final $Z(\theta)$ gate up to an integer multiple of π (similarly, adjust the CNOT gate up to an integer number of $Z(\pi)$ on the control qubit). The remaining gate $Z(n\pi)$ is a Pauli gate, which either a specific hardware operation can implement or the software can keep track of by adapting the remaining computer operations until the next non-Clifford gate is reached.

For CNOT gates, the output of the target buffer mode should, in principle, also be monitored due to the reconvergence phase in which the target mode undergoes significant dynamics. Importantly, the effect of this monitoring—whatever the detection results—is only on the phase of the control qubit. Indeed, the bit degrees of freedom remain exponentially protected on both qubits; and since no operator ever couples to the bit-value information of the target qubit (unlike the control qubit, for which $\mathbf{a} + \mathbf{a}^\dagger$ is sensitive to the bit value), it means that its bit-value information can never leak out in this perfectly monitored scheme and hence no phase-blurring back action can happen on the target qubit. We have indeed verified numerically that, for $\eta = 1$ and no buffer photons detected, an

ideal CNOT gate is retrieved after an infinite time reconvergence by adjusting a $Z(\delta)$ gate on the control qubit with $\delta \ll 1$. A detection on the control-qubit buffer output at time t_J requires an additional $Z(\pi + \delta(t_J))$ gate, as for the previously discussed $Z(\theta)$ gate scheme. In contrast, a detection event on the output of the target buffer mode still requires corrections of order δ only. This is consistent with a first-order Heisenberg-picture analysis as in Sec. III, for which $\mathbf{b}_C$ is proportional to $\sigma_{z,C}$, while $\mathbf{b}_T$ does not carry any qubit information.

APPENDIX F: ADIABATIC ELIMINATION OF THE BUFFER MODE

In Sec. VI, the adiabatic elimination of the buffer mode is performed in the presence of a correlated dissipator. The two-mode master equation is initially given by

$$\frac{d\boldsymbol{\rho}}{dt} = -i\,[\mathbf{H}_{AB}, \boldsymbol{\rho}] + \kappa_{ab}\mathcal{D}[\mathbf{ab}]\boldsymbol{\rho}. \tag{F1}$$

This equation describes an exchange term between cat and buffer modes, as well as a strong correlated dissipation. Here, the fast dynamics correspond to the deexcitation of the buffer mode due to the dissipation term, while the slow dynamics are those of the exchange Hamiltonian. The goal is thus to adiabatically eliminate the fast dynamics when the buffer is excited and to derive an effective single-mode equation for the A mode. Adopting the notation of Ref. [60], we have

$$\begin{aligned} \mathbf{V}_+ &= g_2(\mathbf{a}^2 - \alpha^2)\mathbf{b}^\dagger, \\ \mathbf{V}_- &= g_2^*(\mathbf{a}^{\dagger 2} - \alpha^{*2})\mathbf{b}, \end{aligned} \tag{F2}$$

which are perturbative (de)excitations of the system, $\mathbf{L} = \sqrt{\kappa_{ab}}\mathbf{ab}$ is the jump operator from excited to ground subspaces, and $\mathbf{H}_g = \mathbf{H}_e = 0$ are the block-diagonal Hamiltonians in the ground and excited subspaces. In addition, the non-Hermitian Hamiltonian in the excited subspace reads

$$\mathbf{H}_{\mathrm{NH}} = -\frac{i}{2}\kappa_{ab}\mathbf{a}^\dagger\mathbf{a}\mathbf{b}^\dagger\mathbf{b}\,. \tag{F3}$$

Therefore, the effective single-mode dynamics read

$$\frac{d\boldsymbol{\rho}}{dt} = -i[\mathbf{H}_{\mathrm{eff}}, \boldsymbol{\rho}] + \mathcal{D}[\mathbf{L}_{\mathrm{eff}}]\boldsymbol{\rho}, \tag{F4}$$

where $\mathbf{H}_{\mathrm{eff}} \propto \mathbf{H}_{\mathrm{NH}}^{-1} + \mathbf{H}_{\mathrm{NH}}^{\dagger -1} = 0$ and

$$\begin{aligned} \mathbf{L}_{\mathrm{eff}} &= \mathbf{L}\,(\mathbf{H}_{\mathrm{NH}})^{-1}\,\mathbf{V}_+ \\ &= \frac{2ig_2}{\sqrt{\kappa_{ab}}}\mathbf{a}(\mathbf{a}^\dagger\mathbf{a})^{-1}(\mathbf{a}^2 - \alpha^2). \end{aligned} \tag{F5}$$

This describes a parity-switching jump operator with cat-qubit steady states. In the semiclassical limit, $\mathbf{a}(\mathbf{a}^\dagger\mathbf{a})^{-1} \sim \alpha^{-1}$, such that the effective two-photon dissipation rate is indeed given by $\kappa_2 \equiv 4g_2^2/\alpha^2\kappa_{ab}$.

APPENDIX G: OPTIMIZING THE FLATNESS OF DRIVE HAMILTONIANS

In Sec. VII, we define drive Hamiltonians with odd-power polynomials of the position operator $\mathbf{x}$. For cat-qubit gate engineering, it is required that these high-order drives are locally flat around both cat-qubit coherent components. Mathematically, this corresponds to a minimization of the variance over one coherent state, defined by

$$V_N\,(\{c_n\}) \equiv \frac{1}{\sqrt{2\pi}}\int_{-\infty}^{\infty} H_{Z,N}(x)^2 \mathrm{e}^{-\frac{1}{2}(x-2\alpha)^2} dx, \tag{G1}$$

under the constraint of a fixed mean value of the drive over this coherent state, defined by

$$E_N\,(\{c_n\}) \equiv \frac{1}{\sqrt{2\pi}}\int_{-\infty}^{\infty} H_{Z,N}(x) \mathrm{e}^{-\frac{1}{2}(x-2\alpha)^2} dx, \tag{G2}$$

where $H_{Z,N}(x) = \varepsilon_Z \sum_{n=0}^{N} c_n x^{2n+1}$ is the potential to be optimized, with $N+1$ constants to be determined.

To perform this constrained-minimization problem, we use Lagrange multipliers and define the Lagrangian function as

$$\mathcal{L}_N\,(\{c_n\}, \lambda) = V_N\,(\{c_n\}) - \lambda\,(E_N\,(\{c_n\}) - \varepsilon_0)\,, \tag{G3}$$

where λ is a Lagrange multiplier and ε_0 is the fixed mean value of E_N.

Due to the simple form of Eqs. (G1) and (G2), it is quite simple to find the global minimum of this Lagrangian function exactly. Differentiation of Eq. (G3) with respect to all $N+2$ variables yields

$$\begin{cases} \dfrac{\partial \mathcal{L}_N}{\partial c_k} = 2\displaystyle\sum_{n=0}^{N} I_{2(n+k+1)}c_n - \lambda I_{2k+1}, \\ \dfrac{\partial \mathcal{L}_N}{\partial \lambda} = 1 - \displaystyle\sum_{n=0}^{N} I_{2n+1}c_n, \end{cases} \tag{G4}$$

where we have defined

$$I_k \equiv \frac{1}{\sqrt{2\pi}}\int_{-\infty}^{\infty} x^k \mathrm{e}^{-\frac{1}{2}(x-2\alpha)^2} dx. \tag{G5}$$

Through an integration by parts, a recurrence relation can be obtained for I_k. It reads

$$I_{k+1} = 2\alpha I_k + kI_{k-1}, \tag{G6}$$

with $I_0(\alpha) = 1$ and $I_1(\alpha) = 2\alpha$. As such, I_k is a kth-order polynomial in α. Then, the global minimum of Eq. (G3) is such that $\partial\mathcal{L}_N/\partial c_k = 0$ for all k and $\partial\mathcal{L}_N/\partial\lambda = 0$. This corresponds to a linear set of equations in c_k and λ and can therefore be rewritten as a problem of the form $Ax = y$,

where A is a matrix of the I_k integrals, $x = (c_0, \ldots, c_N, \lambda)$, and $y = (0, 0, \ldots, 0, -1)$. Such a system is easily solved numerically through matrix inversion, thus yielding the solution of the initial problem.

[1] P. W. Shor, Scheme for reducing decoherence in quantum computer memory, Phys. Rev. A **52**, R2493 (1995).

[2] P. W. Shor, in *Proceedings of 37th Conference on Foundations of Computer Science* (IEEE Comput. Soc. Press, 1996).

[3] D. G. Cory, M. D. Price, W. Maas, E. Knill, R. Laflamme, W. H. Zurek, T. F. Havel, and S. S. Somaroo, Experimental quantum error correction, Phys. Rev. Lett. **81**, 2152 (1998).

[4] J. Kempe, D. Bacon, D. A. Lidar, and K. B. Whaley, Theory of decoherence-free fault-tolerant universal quantum computation, Phys. Rev. A **63**, 042307 (2001).

[5] D. Bacon, Operator quantum error-correcting subsystems for self-correcting quantum memories, Phys. Rev. A **73**, 012340 (2006).

[6] A. G. Fowler, M. Mariantoni, J. M. Martinis, and A. N. Cleland, Surface codes: Towards practical large-scale quantum computation, Phys. Rev. A **86**, 032324 (2012).

[7] I. L. Chuang and R. Laflamme, Quantum error correction by coding, arXiv preprint arXiv:quant-ph/9511003 (1995).

[8] Z. Chen, K. J. Satzinger, J. Atalaya, A. N. Korotkov, A. Dunsworth, and D. Sank *et lal.*, Exponential suppression of bit or phase flip errors with repetitive error correction, Nature **595**, 383 (2021).

[9] J. P. B. Ataides, D. K. Tuckett, S. D. Bartlett, S. T. Flammia, and B. J. Brown, The XZZX surface code, Nat. Commun. **12**, 2172 (2021).

[10] R. Acharya, I. Aleiner, R. Allen, T. I. Andersen, M. Ansmann, and F. Arute *et lal.*, Suppressing quantum errors by scaling a surface code logical qubit, Nature **614**, 676 (2023).

[11] Y. Nakamura, Y. A. Pashkin, and J. Tsai, Coherent control of macroscopic quantum states in a single-Cooper-pair box, Nature **398**, 786 (1999).

[12] D. Vion, A. Aassime, A. Cottet, P. Joyez, H. Pothier, C. Urbina, D. Esteve, and M. H. Devoret, Manipulating the quantum state of an electrical circuit, Science **296**, 886 (2002).

[13] J. Koch, T. M. Yu, J. Gambetta, A. A. Houck, D. I. Schuster, J. Majer, A. Blais, M. H. Devoret, S. M. Girvin, and R. J. Schoelkopf, Charge-insensitive qubit design derived from the Cooper pair box, Phys. Rev. A **76**, 042319 (2007).

[14] A. Wallraff, D. I. Schuster, A. Blais, L. Frunzio, J. Majer, M. H. Devoret, S. M. Girvin, and R. J. Schoelkopf, Approaching unit visibility for control of a superconducting qubit with dispersive readout, Phys. Rev. Lett. **95**, 060501 (2005).

[15] A. Blais, A. L. Grimsmo, S. M. Girvin, and A. Wallraff, Circuit quantum electrodynamics, Rev. Mod. Phys. **93**, 025005 (2021).

[16] S. Krinner, N. Lacroix, A. Remm, A. Di Paolo, E. Genois, C. Leroux, C. Hellings, S. Lazar, F. Swiadek, J. Herrmann, G. J. Norris, C. K. Andersen, M. Müller, A. Blais, C. Eichler, and A. Wallraff, Realizing repeated quantum error correction in a distance-three surface code, Nature **605**, 669 (2022).

[17] S. Lloyd and J.-J. E. Slotine, Analog quantum error correction, Phys. Rev. Lett. **80**, 4088 (1997).

[18] D. Gottesman, A. Kitaev, and J. Preskill, Encoding a qubit in an oscillator, Phys. Rev. A **64**, 012310 (2001).

[19] M. H. Michael, M. Silveri, R. T. Brierley, V. V. Albert, J. Salmilehto, L. Jiang, and S. M. Girvin, New class of quantum error-correcting codes for a bosonic mode, Phys. Rev. X **6**, 031006 (2016).

[20] B. M. Terhal, J. Conrad, and C. Vuillot, Towards scalable bosonic quantum error correction, Quantum Sci. Technol. **5**, 043001 (2020).

[21] P. Campagne-Ibarcq, A. Eickbusch, S. Touzard, E. Zalys-Geller, N. E. Frattini, V. V. Sivak, P. Reinhold, S. Puri, S. Shankar, R. J. Schoelkopf, L. Frunzio, M. Mirrahimi, and M. H. Devoret, Quantum error correction of a qubit encoded in grid states of an oscillator, Nature **584**, 368 (2020).

[22] V. V. Albert, S. O. Mundhada, A. Grimm, S. Touzard, M. H. Devoret, and L. Jiang, Pair-cat codes: Autonomous error-correction with low-order nonlinearity, Quantum Sci. Technol. **4**, 035007 (2019).

[23] C. Vuillot, H. Asasi, Y. Wang, L. P. Pryadko, and B. M. Terhal, Quantum error correction with the toric Gottesman-Kitaev-Preskill code, Phys. Rev. A **99**, 032344 (2019).

[24] A. S. Darmawan, B. J. Brown, A. L. Grimsmo, D. K. Tuckett, and S. Puri, Practical quantum error correction with the XZZX code and Kerr-cat qubits, PRX Quantum **2**, 030345 (2021).

[25] K. Noh, C. Chamberland, and F. G. Brandão, Low-overhead fault-tolerant quantum error correction with the surface-GKP code, PRX Quantum **3**, 010315 (2022).

[26] D. S. Schlegel, F. Minganti, and V. Savona, Quantum error correction using squeezed Schrödinger cat states, Phys. Rev. A **106**, 022431 (2022).

[27] T. Hillmann and F. Quijandria, Quantum error correction with dissipatively stabilized squeezed cat qubits, Phys. Rev. A **107**, 032423 (2023).

[28] S. Kwon, S. Watabe, and J.-S. Tsai, Autonomous quantum error correction in a four-photon Kerr parametric oscillator, npj Quantum Inf. **8**, 40 (2022).

[29] P. T. Cochrane, G. J. Milburn, and W. J. Munro, Macroscopically distinct quantum-superposition states as a bosonic code for amplitude damping, Phys. Rev. A **59**, 2631 (1999).

[30] M. Mirrahimi, Z. Leghtas, V. V. Albert, S. Touzard, R. J. Schoelkopf, L. Jiang, and M. H. Devoret, Dynamically protected cat-qubits: A new paradigm for universal quantum computation, New J. Phys. **16**, 045014 (2014).

[31] S. Puri, S. Boutin, and A. Blais, and Engineering the quantum states of light in a Kerr-nonlinear resonator by two-photon driving, npj Quantum Inf. **3**, 18 (2017).

[32] S. Puri, A. Grimm, P. Campagne-Ibarcq, A. Eickbusch, K. Noh, G. Roberts, L. Jiang, M. Mirrahimi, M. H. Devoret, and S. M. Girvin, Stabilized cat in a driven nonlinear cavity: A fault-tolerant error syndrome detector, Phys. Rev. X **9**, 041009 (2019).

[33] H. Putterman, J. Iverson, Q. Xu, L. Jiang, O. Painter, F. G. S. L. Brandão, and K. Noh, Stabilizing a bosonic qubit

using colored dissipation, Phys. Rev. Lett. **128**, 110502 (2021).
[34] D. Ruiz, R. Gautier, J. Guillaud, and M. Mirrahimi, Two-photon driven Kerr quantum oscillator with multiple spectral degeneracies, Phys. Rev. A **107**, 042407 (2023).
[35] Z. Leghtas, S. Touzard, I. M. Pop, A. Kou, B. Vlastakis, A. Petrenko, K. M. Sliwa, A. Narla, S. Shankar, M. J. Hatridge, M. Reagor, L. Frunzio, R. J. Schoelkopf, M. Mirrahimi, and M. H. Devoret, Confining the state of light to a quantum manifold by engineered two-photon loss, Science **347**, 853 (2015).
[36] J. Guillaud and M. Mirrahimi, Repetition cat qubits for fault-tolerant quantum computation, Phys. Rev. X **9**, 041053 (2019).
[37] C. Chamberland, K. Noh, P. Arrangoiz-Arriola, E. T. Campbell, C. T. Hann, J. Iverson, H. Putterman, T. C. Bohdanowicz, S. T. Flammia, A. Keller, G. Refael, J. Preskill, L. Jiang, A. H. Safavi-Naeini, O. Painter, and F. G. Brandão, Building a fault-tolerant quantum computer using concatenated cat codes, PRX Quantum **3**, 010329 (2022).
[38] J. Guillaud and M. Mirrahimi, Error rates and resource overheads of repetition cat qubits, Phys. Rev. A **103**, 042413 (2021).
[39] J. Guillaud, J. Cohen, and M. Mirrahimi, *Quantum Computation with cat Qubits* (Les Houches lecture notes, 2022).
[40] P. Zapletal, A. Nunnenkamp, and M. Brunelli, Stabilization of multimode Schrödinger cat states via normal-mode dissipation engineering, PRX Quantum **3**, 010301 (2022).
[41] L. Gravina, F. Minganti, and V. Savona, A critical dissipative Schrödinger cat qubit, PRX Quantum **4**, 020337 (2023).
[42] R. Lescanne, M. Villiers, T. Peronnin, A. Sarlette, M. Delbecq, B. Huard, T. Kontos, M. Mirrahimi, and Z. Leghtas, Exponential suppression of bit-flips in a qubit encoded in an oscillator, Nat. Phys. **16**, 509 (2020).
[43] C. Berdou, A. Murani, U. Reglade, W. Smith, M. Villiers, J. Palomo, M. Rosticher, A. Denis, P. Morfin, and M. Delbecq *et lal.*, One hundred second bit-flip time in a two-photon dissipative oscillator, arXiv preprint arXiv:2204.09128 (2022).
[44] S. Touzard, A. Grimm, Z. Leghtas, S. O. Mundhada, P. Reinhold, C. Axline, M. Reagor, K. Chou, J. Blumoff, K. M. Sliwa, S. Shankar, L. Frunzio, R. J. Schoelkopf, M. Mirrahimi, and M. H. Devoret, Coherent oscillations inside a quantum manifold stabilized by dissipation, Phys. Rev. X **8**, 021005 (2018).
[45] S. Puri, L. St-Jean, J. A. Gross, A. Grimm, N. E. Frattini, P. S. Iyer, A. Krishna, S. Touzard, L. Jiang, A. Blais, S. T. Flammia, and S. M. Girvin, Bias-preserving gates with stabilized cat qubits, Sci. Adv. **6**, eaay5901 (2020).
[46] A. Grimm, N. E. Frattini, S. Puri, S. O. Mundhada, S. Touzard, M. Mirrahimi, S. M. Girvin, S. Shankar, and M. H. Devoret, Stabilization and operation of a Kerr-cat qubit, Nature **584**, 205 (2020).
[47] K. Mizuno, T. Takenaka, I. Mahboob, and S. Saito, Effect of decoherence for gate operations on a superconducting bosonic qubit, New J. Phys. **25**, 033007 (2023).
[48] F.-M. L. Régent, C. Berdou, Z. Leghtas, J. Guillaud, and M. Mirrahimi, High-performance repetition cat code using fast noisy operations, arXiv preprint arXiv:2212.11927 (2022).
[49] Q. Xu, J. K. Iverson, F. G. S. L. Brandão, and L. Jiang, Engineering fast bias-preserving gates on stabilized cat qubits, Phys. Rev. Res. **4**, 013082 (2022).
[50] R. Gautier, A. Sarlette, and M. Mirrahimi, Combined dissipative and hamiltonian confinement of cat qubits, PRX Quantum **3**, 020339 (2022).
[51] Q. Xu, G. Zheng, Y.-X. Wang, P. Zoller, A. A. Clerk, and L. Jiang, Autonomous quantum error correction and fault-tolerant quantum computation with squeezed cat qubits, arXiv preprint arXiv:2210.13406 (2022).
[52] R. Azouit, F. Chittaro, A. Sarlette, and P. Rouchon, Towards generic adiabatic elimination for bipartite open quantum systems, Quantum Sci. Technol. **2**, 044011 (2017).
[53] P. Forni, A. Sarlette, T. Capelle, E. Flurin, S. Deléglise, and P. Rouchon, Adiabatic elimination for multi-partite open quantum systems with non-trivial zero-order dynamics, 2018 IEEE Conference on Decision and Control (CDC), 6614 (2018).
[54] H.-P. Breuer and F. Petruccione *et lal.*, *The Theory of Open Quantum Systems* (Oxford University Press, 2007).
[55] D. A. Steck, Quantum and atom optics (2006).
[56] E. Albertinale, L. Balembois, E. Billaud, V. Ranjan, D. Flanigan, T. Schenkel, D. Estève, D. Vion, P. Bertet, and E. Flurin, Detecting spins by their fluorescence with a microwave photon counter, Nature **600**, 434 (2021).
[57] R. Dassonneville, R. Assouly, T. Peronnin, P. Rouchon, and B. Huard, Number-resolved photocounter for propagating microwave mode, Phys. Rev. Appl. **14**, 044022 (2020).
[58] R. Lescanne, S. Deléglise, E. Albertinale, U. Réglade, T. Capelle, E. Ivanov, T. Jacqmin, Z. Leghtas, and E. Flurin, Irreversible qubit-photon coupling for the detection of itinerant microwave photons, Phys. Rev. X **10**, 021038 (2020).
[59] J. M. Gertler, S. v. Geldern, S. Shirol, L. Jiang, and C. Wang, Experimental realization and characterization of stabilized pair coherent states, PRX Quantum **4**, 020319 (2023).
[60] F. Reiter and A. S. Sørensen, Effective operator formalism for open quantum systems, Phys. Rev. A **85**, 032111 (2012).
[61] Here, we use the mathematical equivalence with a mechanical harmonic oscillator, to call position x and momentum p the real and imaginary quadratures of the electromagnetic mode.
[62] This drive Hamiltonian is ideal up to exponentially small corrections, due to the orthonormalization of the computational basis—two coherent states are never exactly orthogonal—or in other words, to the Gaussian tails of coherent states that cross the $x = 0$ line in their phase space distributions.
[63] K. Kumar, A. Vepsäläinen, S. Danilin, and G. Paraoanu, Stimulated Raman adiabatic passage in a three-level superconducting circuit, Nat. Commun. **7**, 1 (2016).
[64] A. Vepsäläinen, S. Danilin, and G. S. Paraoanu, Superadiabatic population transfer in a three-level superconducting circuit, Sci. Adv. **5**, eaau5999 (2019).
[65] J. Cohen, Autonomous quantum error correction with superconducting qubits (2017).
[66] U. Réglade, A. Bocquet, R. Gautier, A. Marquet, E. Albertinale, N. Pankratova, M. Hallen, F. Rautschke, L.-A. Sellem,

P. Rouchon, A. Sarlette, M. Mirrahimi, P. Campagne-Ibarcq, R. Lescanne, S. Jezouin, and Z. Leghtas, Quantum control of dynamical states with switching times exceeding ten seconds, arXiv preprint arxiv:2307.06617 (2023).

[67] N. Cerf and S. Iblisdir, Phase conjugation of continuous quantum variables, Phys. Rev. A **64**, 032307 (2001).

[68] M. M. Wolf and J. I. Cirac, Dividing quantum channels, Commun. Math. Phys. **279**, 147 (2008).